

# ALMA ASTROCHEMICAL OBSERVATIONS OF THE INFRARED-LUMINOUS MERGER NGC 3256

NANASE HARADA,<sup>1</sup> KAZUSHI SAKAMOTO,<sup>1</sup> SERGIO MARTÍN,<sup>2,3</sup> SUSANNE AALTO,<sup>4</sup> REBECA ALADRO,<sup>5</sup>  
AND KAZIMIERZ SLIWA<sup>6</sup>

<sup>1</sup>*Academia Sinica Institute of Astronomy and Astrophysics, P.O. Box 23-141, Taipei 10617, Taiwan*

<sup>2</sup>*European Southern Observatory, Alonso de Córdova 3107, Vitacura, Santiago, Chile*

<sup>3</sup>*Joint ALMA Observatory, Alonso de Córdova 3107, Vitacura, Santiago, Chile*

<sup>4</sup>*Department of Space, Earth and Environment, Chalmers University of Technology, Onsala Space Observatory, SE-43992 Onsala, Sweden*

<sup>5</sup>*Max Planck Institute for Radio Astronomy, Auf dem Hügel 69, D-53121 Bonn, Germany*

<sup>6</sup>*Max Planck Institute for Astronomy, Königstuhl 17, D-69117 Heidelberg, Germany*

## ABSTRACT

In external galaxies, molecular composition may be influenced by extreme environments such as starbursts and galaxy mergers. To study such molecular chemistry, we observed the luminous-infrared galaxy and merger NGC 3256 using the Atacama Large Millimeter/sub-millimeter Array. We covered most of the 3-mm and 1.3-mm bands for a multi-species, multi-transition analysis. We first analyzed intensity ratio maps of selected lines such as HCN/HCO<sup>+</sup>, which shows no enhancement at an AGN. We then compared the chemical compositions within NGC 3256 at the two nuclei, tidal arms, and positions with influence from galactic outflows. We found the largest variation in SiO and CH<sub>3</sub>OH, species that are likely to be enhanced by shocks. Next, we compared the chemical compositions in the nuclei of NGC 3256, NGC 253, and Arp 220; these galactic nuclei have varying star formation efficiencies. Arp 220 shows higher abundances of SiO and HC<sub>3</sub>N than NGC 3256 and NGC 253. Abundances of most species do not show strong correlation with the star formation efficiencies, although the CH<sub>3</sub>CCH abundance seems to have a weak positive correlation with the star formation efficiency. Lastly, the chemistry of spiral arm positions in NGC 3256 is compared with that of W 51, a Galactic molecular cloud complex in a spiral arm. We found higher fractional abundances of shock tracers, and possibly also higher dense gas fraction in NGC 3256 compared with W 51.

*Keywords:* galaxies: individual (NGC 3256), astrochemistry, ISM: molecules, galaxies: starburst, galaxies: ISM, galaxies: abundances

## 1. INTRODUCTION

Molecular composition (or simply “chemistry”) of various species in the interstellar medium (ISM) varies with the environment surrounding the molecular clouds. Although the dominant species in molecular regions is  $\text{H}_2$ , and the second most abundant molecule CO is most commonly observed, more minor species are more sensitive to physical conditions. For example, the compositions of those minor species vary with stages of star formation or external radiation such as UV-photons, X-rays, cosmic-rays, or shocks (see Harada 2017, and references therein). Molecular composition also changes as a molecular cloud evolves from diffuse clouds to form denser cores before the star formation.

Despite faint emission due to large distance, about 60 species have been previously detected in external galaxies<sup>1</sup>. In starburst galaxies, the chemistry is likely to show features of photon-dominated regions (PDRs) due to the high UV-photon flux. At the same time, starburst galaxies may have higher fractions of dense, star-forming gas compared to galaxies with lower star formation rates. If so, this difference in the ISM properties can also affect the chemistry.

Recent development of Atacama Large Millimeter/sub-millimeter Array (ALMA) and some pre-ALMA radio interferometers has opened up the possibility of spatially-resolved astrochemistry in external galaxies (e.g., Meier & Turner 2005; Takano et al. 2014; Viti et al. 2014; Nakajima et al. 2015; Meier et al. 2015; Martín et al. 2015). The chemical compositions seen in those observations vary with types of galaxies. One of the most characteristic chemical compositions is seen in so-called compact obscured nuclei (CONs). CONs are extremely compact ( $< 10$ s of parsecs), obscured ( $A_V > 10^3$  mag),

and luminous ( $> 10^{10} L_\odot$ ) nuclei in some ultra/luminous infrared galaxies (U/LIRGs). For example, Arp 220 and NGC 4418 have CONs, and have very high abundances of  $\text{HC}_3\text{N}$  or  $\text{CH}_3\text{CN}$  (Martín et al. 2011; Costagliola et al. 2015). In the Galaxy, these molecules are usually seen only towards star-forming regions, and their abundances averaged in the galaxy scale are very low. Even in local starburst galaxies such as NGC 253 and M82, these molecules are much less abundant than in CONs. In addition, the CONs have strong emission of vibrationally-excited lines (Sakamoto et al. 2010; Aalto et al. 2015b; Martín et al. 2016) with upper state energies ranging from a few hundreds to  $\sim 1000$  K. Their detections suggest strong infrared radiation for the excitation. Because of the high degree of obscuration, it is still unclear whether these chemical features are caused by extreme starbursts or active galactic nuclei (AGNs), or the compactness of the nuclei.

What the observed chemistry is most sensitive to in external galaxies is still unknown partly because of the lack of previous observations, and partly because of the complexity contained in beams typically of giant molecular cloud sizes or larger. In starburst galaxies, molecular abundances species associated with dense cores could correlate with the current star formation rate, but the correlation may not be tight because the molecular clouds are ingredients of future star formation, and they may be showing different stages from existing massive stars used to measure the star formation rate. This time delay is suggested in the molecular study of NGC 253 by Ando et al. (2017), where the chemistry significantly varies among clumps with similar star formation rates. Another driving force of the chemistry is feedback from the existing stars such as irradiation from UV-photons (e.g., Martín et al. 2009). To understand the mechanisms behind the chemical

<sup>1</sup> <https://www.astro.uni-koeln.de/cdms/molecules>

composition, it is important to observe starburst galaxies with various star formation rates.

NGC 3256 is an ideal target for such a test. NGC 3256 ( $D = 35$  Mpc,  $170\text{pc}/1''$ ) is a late-stage merger (by the definition of merger stage by [Stierwalt et al. \(2013\)](#); two nuclei in a common envelope). An intense starburst caused by the merging activity generates a high infrared luminosity of  $L_{IR} = 3 \times 10^{11} L_{\odot}$ . Star formation rates in the northern and the southern nuclei (N and S nuclei hereafter) are  $15 M_{\odot} \text{ yr}^{-1}$  and  $6 M_{\odot} \text{ yr}^{-1}$  respectively, according to the spectral energy distribution (SED) fitting in the near- and mid-infrared wavelengths ([Lira et al. 2008](#)). The total star-formation rate within this galaxy is estimated to be  $\sim 50 M_{\odot} \text{ yr}^{-1}$  ([Sakamoto et al. 2014](#)), and it is expected that the star formation rate even in the off-nucleus positions should still be much higher compared with local starburst galaxies such as NGC 253 (total SFR  $\sim 5 M_{\odot} \text{ yr}^{-1}$ ).

Although the main energy source of NGC 3256 is known to be the starburst event, there are other interesting features that can be studied in NGC 3256. One of them is the AGN in the S nucleus. The configuration of the southern galaxy is almost edge-on, and the very central part of the S nucleus is highly obscured. Therefore, presence of an AGN in the S nucleus lacked convincing evidence (e.g., [Lira et al. 2002](#)). Recently, [Ohyama et al. \(2015\)](#) have revisited this issue using IR and X-rays, and found that the fit shows an AGN-like feature in the S nucleus. Such AGN/starburst activities are giving feedback to the interstellar medium (ISM) in NGC 3256. From the velocity components shifted from the range expected from the galaxy rotation, outflows are detected in ionized gas ([Leitherer et al. 2013](#)), cold molecular gas ([Sakamoto et al. 2006a, 2014](#)), and hot molecular gas ([Emonts et al. 2014](#)). [Sakamoto et al. \(2014\)](#) found that the energy in the outflow from the N nucleus can be explained by star forma-

tion alone, but the outflow from the S nucleus cannot be accounted for just by a starburst, and needs the presence of an AGN. By studying the chemistry of NGC 3256, we can examine various topics such as the effects of star formation, merging events, and outflows on the molecular compositions.

In this paper, we present a molecular line survey to cover most of the ALMA Bands 3 and 6 to study the chemical abundances at locations within the central kpc of NGC 3256. The organization of this paper is as follows. In Section 2, we explain our observations and analysis. The results obtained from those observations are described in Section 3 for the continuum and molecular lines. Then, the column densities of individual molecules and their ratios are discussed in Section 4. In Section 5, we further discuss the implication of the results in Sections 3 and 4. Finally, we summarize our findings in Section 6.

## 2. OBSERVATIONS

Our ALMA observations (project code 2015.1.00412.S and 2016.1.00965.S) span through Cycles 3 and 4 using the 12-meter array and Atacama Compact Array (ACA) for higher-frequency observations. The observation parameters are summarized in Table 1. For the better signal-to-noise (S/N) ratio, we also used the ALMA data 2015.1.00993.S in the archive for frequency ranges overlapping with ours. To get the data on the CN (1 – 0) line, we also used the ALMA data 2011.0.00525.S, whose observational parameters are described in [Sakamoto et al. \(2014\)](#). Our observations covered most of Bands 3 and 6. For calibration, we ran the pipeline calibration script using *CASA* version 4.5.3 for cycle 3 data and version 4.7 for cycle 4 data. Then, we checked the amplitude and phase stability of the pipelined data, and no major problem was found. We note that the calibrator of the scheduling block B6\_h taken in cycle 4 has fluctuation near

the atmospheric absorption at 258 GHz and 271 GHz because the frequency dependence of  $T_{\text{sys}}$  there was not accurately corrected due to channel smoothing. Since this fluctuation only affects specific frequencies and there is no lines of interest around these frequencies, we proceed with those calibrated data. To improve the accuracy of flux calibration, we corrected the flux using the continuum fluxes as follows. Continuum flux values at both nuclei were plotted as a function of frequency. Then, we fitted them with the power law  $\nu^\alpha$  ( $\nu$ : frequency) for Band 3 and Band 6 separately. We determined the scaling factor for each sideband and each nucleus to match the power law fit. By taking the average of scaling factors between both sidebands and nuclei, we determined the degree of correction for the amplitude error. We applied this correction to scheduling blocks with more than 3% discrepancy from the power law fit. Our resulting flux errors should be within  $\sim 5\%$ . Imaging and simple image analysis were done with *CASA* version 4.6. Missing fluxes were evaluated by comparing the images with ACA and without ACA. Since we do not have ACA data for all the scheduling blocks, we used HCN(3 – 2), HCO<sup>+</sup>(3 – 2), and C<sup>18</sup>O(2 – 1) for this comparison, and the estimated missing fluxes are 4.7 %, 0.2 %, and 2.8 %, respectively. We do not have the ACA data for <sup>13</sup>CO, and the missing flux is expected to be higher for this line because of the extended emission.

### 3. OBSERVATIONAL RESULTS

Before we explain our results later in this section, we briefly explain the morphology of NGC 3256 for clarity. In NGC 3256, the two nuclei, N and S nuclei are indicated as “N” and “S” in Figure 1 (*left*). Spiral arm positions are indicated as “C” (central peak), “TNE” (tidal arm northeast), “TSE” (tidal arm southeast),

“TSW” (tidal arm southwest)<sup>2</sup>. The position of the outflow from the S galaxy is indicated as “OS” (outflow south). There is also a peak at western part of the S galaxy (south galaxy west indicated as “SW”). At position OS and around position C, there are components red-shifted blue-shifted from the systemic velocity (Figure 1 *middle*), which are thought as outflow components. These high-velocity components were already found with CO by Sakamoto et al. (2014) at similar positions. A proposed image for this galaxy merger system similar to the one in Sakamoto et al. (2014) is shown in Figure 1 (*right*).

#### 3.1. Continuum Emission

Continuum images at  $\lambda = 3.0$  mm and 1.2 mm are shown in Figure 2. Images at these two wavelengths are similar to each other, and to continuum images at 2.81 mm, 0.86 mm in Sakamoto et al. (2014). Those images are overall similar to the radio continuum image at 3.6 cm by Neff et al. (2003), but only the 3.6-cm image has the feature south from the southern galaxy at the position of outflow from the S nucleus (see Figure 16 of Sakamoto et al. 2014, for the 3.6-cm feature at the position of the outflow). Spectral indices  $\alpha$  of N and S nuclei where  $S_\nu \propto \nu^\alpha$  are derived using the continuum data using each scheduling block in each sideband. We use only the PI data (2015.1.00412.S and 2016.1.00975.S) for the fit, and the fits were obtained for Band 3 and Band 6 separately. Continuum flux densities within 2'' are plotted in Figure 3. Each sideband has a 1.875-GHz width, and the frequency ranges of each sideband can be found in Table 1. Those values are

<sup>2</sup> Although it is likely that those arms are influenced by the tidal interaction, we note that all the spiral arms may not have the tidal origin. It is known from simulations and observations that galaxy mergers can create such arm-like features through tidal interaction (e.g., D’Onghia et al. 2010; Haan et al. 2011).

obtained after convolving all the images to  $2.0''$ . For the northern nucleus,  $\alpha = -0.39 \pm 0.10$  for Band 3, and  $\alpha = 1.99 \pm 0.09$  for Band 6. The value in the southern nucleus is equivalent to the northern nucleus in Band 3 ( $\alpha = -0.37 \pm 0.08$ ), but the one for Band 6 is lower than the northern nucleus ( $\alpha = 1.16 \pm 0.10$ ). Values obtained from  $f_{\text{obs}} = 85.5 - 110.3$  GHz are lower than the ones obtained from  $f_{\text{obs}} = 99.6 - 115.0$  GHz by Sakamoto et al. (2014), which are  $-0.12$  for northern nucleus and  $-0.19$  for southern nucleus. This is reasonable because there should be more contribution from Synchrotron radiation ( $\alpha \sim -1$ ) than the contribution from free-free emission ( $\alpha \sim -0.1$ ) at the lower frequency. At the same time, this level of change in  $\alpha$  can be easily caused by the flux error, which seems to be a more likely cause (see Figure 3). Similarly, values of  $\alpha$  at  $\lambda = 0.86$  mm in Sakamoto et al. (2014) are higher than the ones at  $\lambda = 1.2$  mm because the dust emission ( $\alpha \sim 3 - 4$ ) has more contribution at the higher frequency.

### 3.2. Molecular line images

Velocity-integrated moment maps of selected molecular lines and a radio recombination line (H40 $\alpha$ ) are shown in Figures 4 and 5. In those images, the primary beam is not corrected. The sizes of primary beams are  $\frac{51.5''}{100(\text{GHz})}$ , and most of the emission is within  $10''$ . For each transition and without taking line blending into account, we integrated the velocity range  $\pm 165$  km s $^{-1}$  around the transition to produce the moment 0 maps. Image parameters and rms values of those images are listed in Table 2. For molecules with doublet or triplet transitions such as CN or CCH, we integrated velocity ranges of all transitions. Main structures such as the two nuclei, tidal arms, and the outflow (see Figure 1 right for a schematic image) are well traced by major lines such as  $^{13}\text{CO}$ ,  $\text{C}^{18}\text{O}$ , HCN, and  $\text{HCO}^+$ , while weaker molecular lines are detected only in selected positions. Spa-

tial distribution of emission intensities of some molecular lines are obviously different from that of CO isotopologues. For example, the distribution of SiO(2-1) is enhanced in the position between the two nuclei and the southwest tidal arm position (Figure 5). The integrated intensity maps of methanol ( $\text{CH}_3\text{OH}$ ) also have different distributions from that of CO isotopologues although transitions at 96.7 GHz and around 241 GHz have different distribution to each other as well (Figure 5). For both transitions of methanol, emission at the two nuclei is not dominant, and emission from tidal arms or the outflow is more visible. For the transition at 96.7 GHz, the emission from the northern nucleus is not obvious while it is visible in 241 GHz. Another molecule with significantly different distribution from CO isotopologues is  $\text{N}_2\text{H}^+$ . While other molecules have some contribution from the both nuclei,  $\text{N}_2\text{H}^+$  is very weak in the S nucleus. Those features mentioned here will be quantitatively analyzed and discussed in Section 4.

#### 3.2.1. Ratio maps

Spatial variations of intensity ratios are more clearly shown in the ratio maps. In Figure 6, ratios of molecular emission intensities in Kelvin units are shown. Primary beams are corrected for each moment 0 maps before the ratios are taken to produce these images. The  $\text{HCN}(1-0)/^{13}\text{CO}(1-0)$  ratio is higher in the N nucleus than in the S nucleus (Figure 6, left). This ratio is also high at the outflow position of the southern galaxy. The  $\text{HCN}(1-0)/\text{HCO}^+(1-0)$  ratio is  $\sim 1.0$  in the N nucleus while  $\sim 0.6$  in the S nucleus, and it is lower in the S nucleus than in the N nucleus. This  $\text{HCN}(1-0)/\text{HCO}^+(1-0)$  ratio has been suggested as the AGN/starburst diagnostics first by Kohno et al. (2001), and later followed up by Izumi et al. (2016) and Privon et al. (2017). Results by Kohno et al. (2001) ( $\text{HCN}/\text{HCO}^+$  for  $J = 1 - 0$ ) and Izumi et al. (2016)



(HCN/HCO<sup>+</sup> for  $J = 4 - 3$  and HCN(4 - 3)/CS(7 - 6)) show the values of HCN/HCO<sup>+</sup> or HCN/CS are lower in the starburst galaxies (HCN/HCO<sup>+</sup> < 1 for both transitions) than in AGN-containing galaxies (HCN/HCO<sup>+</sup>  $\sim 1 - 3$ ). At the same time, Izumi et al. (2016) pointed out that the high-resolution data of AGN-containing galaxies do not show enhanced HCN(1 - 0)/HCO<sup>+</sup>(1 - 0) at the location of AGNs (see also García-Burillo et al. 2014; Martín et al. 2015, for the data in the individual galaxies). On the other hand, Privon et al. (2017) found that there is no significant difference between starburst and AGN-containing galaxies for the sample of LIRGs, possibly due to the high opacity. Even for LIRGs, Imanishi & Nakanishi (2014) argued that AGNs show elevated HCN(4 - 3)/HCO<sup>+</sup>(4 - 3) ratios in their ALMA observations. In NGC 3256, S nucleus is the one that shows the past activity of AGN activity although it has the lower HCN(1 - 0)/HCO<sup>+</sup>(1 - 0) ratio showing the opposite trend from the AGN/starburst diagnostics mentioned above. The ratios in the both nuclei are within the range of values in typical starburst galaxies. Even in AGN-containing galaxies, the line ratios may become similar to those in starburst galaxies if the beam sizes are too large. However, it is unlikely that the observed ratios in NGC 3256 from our observations show starburst-like line ratios of HCN(1 - 0)/HCO<sup>+</sup>(1 - 0) simply because of the beam smearing. The beam size of our ratio map is 230 pc, which is equivalent to or smaller than beam sizes in Kohno et al. (2001) and “high-resolution samples” in Izumi et al. (2016). Although we cannot make direct comparison with line ratios for different transitions, both HCN(1 - 0)/HCO<sup>+</sup>(1 - 0) and HCN(1 - 0)/CS(2 - 1) show similar ratio to values of HCN(4 - 3)/HCO<sup>+</sup>(4 - 3) and HCN(4 - 3)/CS(7 - 6) for samples of starburst galaxies shown in Izumi et al. (2016). The intensity ra-

tios of HNC(1 - 0)/HCN(1 - 0) do not differ significantly between the N and S nuclei. Variation of these ratios reflect either the change in molecular abundances or excitation.

Some features can be attributed to the change in the excitation and critical densities. For example, if the mean density in the N nucleus is higher than the S nucleus, it can explain the higher HCN(1-0)/<sup>13</sup>CO(1 - 0) and the higher HCN(1 - 0)/HCO<sup>+</sup>(1 - 0) ratios in the N nucleus. The critical densities of <sup>13</sup>CO, HCO<sup>+</sup>, HCN for  $J = 1 - 0$  transitions are  $n_{\text{crit}} \sim 2 \times 10^3 \text{ cm}^{-3}$ ,  $2 \times 10^5 \text{ cm}^{-3}$ , and  $1 \times 10^6 \text{ cm}^{-3}$ , respectively <sup>3</sup>.

On the other hand, the HNC(1 - 0)/HCN(1 - 0) ratios cannot be explained solely by the excitation. The critical density of HNC(1 - 0) is  $n_{\text{crit}} \sim 3 \times 10^5 \text{ cm}^{-3}$ , and the HNC(1 - 0)/HCN(1 - 0) ratio should be lower in the N nucleus if the critical density is the only contributing factor. It has been pointed out that molecules emit at densities 1-2 orders of magnitudes lower than critical densities (Shirley 2015), and also that the distribution of molecular emission within GMCs do not vary as expected from critical density alone due to both excitation and chemical abundances (Pety et al. 2017; Kauffmann et al. 2017; Watanabe et al. 2017; Nishimura et al. 2017). Watanabe et al. (2017) and Nishimura et al. (2017) examined the fractions of molecular line intensities coming from extended diffuse components and denser star forming regions in Galactic GMCs. Among species mentioned above, <sup>13</sup>CO, HCN, HCO<sup>+</sup>, and HNC, their results suggest that <sup>13</sup>CO emis-

<sup>3</sup> Critical densities listed here are estimated by simply assuming the two level approximation without considering the photon trapping and take  $n_{\text{crit}} = A_{ul}/\gamma_{ul}$  where  $A_{ul}$  is the Einstein A coefficient for a transition from the level  $u$  and to the level  $l$ ,  $\gamma_{ul}$  is a collisional coefficient for a transition from the level  $u$  and to the level  $l$ . Values of  $A_{ul}$  and  $\gamma_{ul}$  were obtained from Leiden Atomic and Molecular Database (Schöier et al. 2005). The temperature of 10 K was assumed for  $\gamma_{ul}$ .

sion has more contribution from more extended regions, HCN and  $\text{HCO}^+$  emission from more compact regions, and HNC has the highest contribution from the compact star-forming regions probably from dense, yet still cold gas. If distribution of molecular emission in the nuclei of NGC 3256 is similar to that of Galactic GMCs, the observed line ratios can be explained if the N nucleus has more fraction of dense and compact clouds than in the S nucleus. However, we should also note that [Meier & Turner \(2005\)](#) did not see any temperature dependence of HNC/HCN intensity ratio in a starburst galaxy IC 342 possibly because of the high opacity. Another explanation of the lack of temperature dependence is from the high ionization rate, which can create higher abundance of  $\text{HCNH}^+$  to form HNC through the recombination with an electron ([Aalto et al. 2002](#)).

Another feature to note is the higher  $\text{HCN}(1-0)/^{13}\text{CO}(1-0)$  ratio in the outflow position. It is surprising if it is due to the higher density in the outflow because outflows are usually considered to be hot and tenuous. This feature might be a reflection of higher fractional abundance<sup>4</sup> of HCN due to the higher gas temperature ([Loenen et al. 2008](#); [Harada et al. 2010](#)) possibly due to shocks ([Aalto et al. 2012](#); [Martín et al. 2015](#); [Izumi et al. 2016](#)). Higher  $\text{HCN}(1-0)/\text{CS}(2-1)$  and lower  $\text{HNC}(1-0)/\text{HCN}(1-0)$  also supports this scenario. On the other hand, the  $\text{HCN}(1-0)/\text{HCO}^+(1-0)$  do not show strong enhancement at the outflow position. It is possible that  $\text{HCO}^+$  is also enhanced due to ionization in the outflow, but the precise density structure and molecular abun-

dances need to be further explored. However, this enhancement may also be due to the higher density, similar to the case of the outflow in Mrk 231 ([Aalto et al. 2015a](#)).

### 3.3. Molecular spectra

To analyze individual positions of interest, we extracted spectra from our image cubes. For this analysis, we use the primary-beam corrected cubes. Since we did not have the ACA data for all the Band 6 scheduling blocks, we only used the 12-meter data for consistency. The spectra used to calculate column densities in the next section are produced by convolving the image cubes to a common  $1.7''$  resolution. The rms values of individual spectral windows are listed in Table 3. To include the  $\text{CN}(1-0)$  line in the analysis, we also used the data produced for [Sakamoto et al. \(2014\)](#). The positions we analyzed are shown in Figure 1 (*left*) as discussed at the beginning of Section 3 (N: northern nucleus, S: southern nucleus, C: central peak, TNE: tidal arm northeast, TSE: tidal arm southeast, TSW: tidal arm southwest, OS: outflow south, SW: southern galaxy west). Note that in the analysis of column densities in the later sections, we use the entire velocity range around the systemic velocity for the position OS, and it may have some contamination from non-outflow components is possible. Plots of spectra are shown in Figures 16 - 19 for the position N (see the online journal of the published version for all positions). Observed peak intensities and integrated intensities are listed in Table 13 for detected species and tentatively detected species with  $> 2\sigma$  at the peak. The integrated intensities are calculated by integrating a velocity range of  $\pm 150 \text{ km s}^{-1}$  from the systemic velocity of  $2775 \text{ km s}^{-1}$ . Errors for the integrated intensities are estimated as  $\Delta I \Delta v \sqrt{N}$  where  $\Delta I$  is the rms of the original cube corrected according to the position in the primary beam,  $\Delta v$  is the velocity resolution of the cube, and  $N = v_{\text{range}}/\Delta v$  for  $v_{\text{range}} = 300 \text{ km s}^{-1}$ . If

<sup>4</sup> Fractional abundances refer to abundances of certain species over total hydrogen or molecular hydrogen abundances. In this paper, we discuss the variation of fractional abundances from abundances of certain species over some reference species such as  $^{13}\text{CO}$  or CS because of the difficulty of obtaining the total hydrogen abundances.

lines are narrower than  $v_{range} = 300 \text{ km s}^{-1}$ , the actual errors may be smaller. That is why some of weak lines have low values of  $I\Delta V$ .

While the molecular line spectra can be fit with a single Gaussian profile in most positions, there are exceptions. For example, spectrum shapes of the N and S nuclei have double peaks for most of the species. It is likely that these double peaks come from the rotation of the galactic nuclei, and not from self absorption because even molecules that are thought to be optically thin have double peaks. Another position where spectra cannot be fit well with a single gaussian is the position OS, which can be explained by the complicated velocity structure of the outflow. Line wings from the outflow are detected clearly at the peak position of the red-shifted component seen in Figure 1 (*middle*) for HCN(1 – 0), HCO<sup>+</sup>(1 – 0), and HNC(1 – 0) shown in Figure 7.

#### 4. COLUMN DENSITIES

To quantify the spatial variation of the chemical composition, we present the column densities of detected species in this section using the spectra presented in Section 3.3. To obtain column densities, we used a spectral fitting feature of MADCUBA (Martín et al., in preparation)<sup>5</sup>. In this program, the fit between the simulated spectra and the observed one is calculated, and column densities and excitation temperatures with the best fit can be obtained under the LTE approximation. In the simulated spectra, optical depth is also taken into account. The list of obtained column densities and excitation temperatures are listed in Tables 5 - 12. Errors shown in those tables are errors from the fitting. The estimated  $T_{ex}$  are mostly  $\lesssim 10 \text{ K}$  except for HC<sub>3</sub>N, CH<sub>3</sub>CCH, CH<sub>3</sub>OH, and H<sub>2</sub>CO. For those molecules,  $T_{ex}$  can be as high as 20-40 K. For a molecule with only one line with enough S/N,

we used  $T_{ex} = 10 \text{ K}$ . Even with the detection of multiple transitions, there are cases where  $T_{ex}$  cannot be precisely determined. For those cases,  $T_{ex}$  was fixed at the best-fit value to obtain column densities. If the molecular species are undetected at certain positions, the upper limits are obtained by deriving column densities for cases of 2- $\sigma$  detections at the lowest (or strongest) transition with  $T_{ex} = 10 \text{ K}$ .

In the following sections, we plot the ratios of the derived column densities. We use two different species with different critical densities (<sup>13</sup>CO and CS) as denominator of the ratios for the following reasons. Since we have detections of multiple transitions for most of the major species, the derived column densities should result from differences in fractional abundances. However, this is not always the case if the density distribution within the beam is different. If the beam contains higher fraction of relatively dense material, then molecules with higher critical densities have a larger area/volume where they can emit. This higher fraction of dense gas can result in higher apparent abundances even when the abundances are derived using multiple transitions. If this excitation factor plays a role in the ratio of column densities, discussion of variation of fractional abundances are only valid when the column density ratios are obtained using molecules with similar critical densities for both numerator and denominator. <sup>13</sup>CO is a good denominator for molecules with low critical densities while CS is suitable for high  $n_{crit}$  molecules. We have already mentioned in Section 3.2.1 that molecules may emit at lower densities than the critical densities, but molecules such as CS still emit more effectively at higher densities than <sup>13</sup>CO (Watanabe et al. 2017; Nishimura et al. 2017).

##### 4.1. Comparison within NGC 3256

We first compare the chemistry among the 8 positions we analyzed in NGC 3256. Here we focus our discussion on selected species

<sup>5</sup> <http://cab.inta-csic.es/madcuba/Portada.html>



such as species with higher critical densities (HCN,  $\text{HCO}^+$ , CS, and CN), species enhanced with shocks (SiO,  $\text{CH}_3\text{OH}$ , HNC), species enhanced in PDRs (CCH,  $\text{HOC}^+$ ), and species seen in cold dense cores ( $\text{N}_2\text{H}^+$ ). We also discuss  $\text{CH}_3\text{CCH}$  because it was proposed to be AGN/starburst diagnostics by [Aladro et al. \(2015\)](#). We omit discussion of species detected in 3 or less positions (c- $\text{C}_3\text{H}_2$ ,  $\text{CH}_3\text{CN}$ , and  $\text{CO}^+$ ), some isotopologues ( $\text{H}^{13}\text{CO}^+$  and  $\text{C}^{34}\text{S}$ ), and species with little variation among positions (SO, NO, and  $\text{H}_2\text{CO}$ ). We arrange the column density ratios by CS column densities in the descending order in Figures 8 - 9.

In Figure 8 (top), column density ratios of molecules with relatively high critical densities over  $^{13}\text{CO}$  are plotted in the log scale. To highlight the variation among the locations, the column density ratios over  $^{13}\text{CO}$  normalized to the value at the location “N” are shown in Figure 8 (bottom) also in the log scale. Variation of column density ratios seem similar among molecules. Although it is possible that the fractional abundances of those molecules vary among those positions in a similar way, it is likely that the variation of excitation condition within the beam discussed earlier in Section 4 is changing those apparent fractional abundances.

On the other hand, there is variation of derived column density ratios that is likely caused by differences in fractional abundances of certain molecules. Behavior of such molecules are described below, and column densities are plotted in Figure 9.

**SiO:** The column density ratios of SiO over  $^{13}\text{CO}$  and over CS show both enhancement at the position OS. Silicon monoxide is expected to be enhanced in strong shocks of velocity  $v_{\text{shock}} > 25 \text{ km s}^{-1}$  ([Gusdorf et al. 2008](#)) due to sputtering from the dust core. Although it was claimed that there is a correlation between SiO intensity and X-ray strength ([Amo-Baladrón et al. 2009](#)), this correlation is a weak one. It is indeed the-

oretically possible that X-ray heats up the dust enough to make it sublime, SiO as an XDR tracer should be taken with a caution. If this outflow is an AGN-induced outflow, both shocks and X-rays are naturally expected.

**$\text{CH}_3\text{OH}$ :** Column density ratios of  $\text{CH}_3\text{OH}$  vary in a similar way to that of SiO although the enhancement at one of the tidal arm positions (TSW) is also prominent for  $\text{CH}_3\text{OH}$ .  $\text{CH}_3\text{OH}$  is known to be enhanced in weak shocks. For methanol, there are other mechanisms to increase its abundance in the gas-phase such as cosmic-ray or UV-induced photo-desorption, or chemical desorption. However, chemical desorption should affect the larger galactic scale, and cannot explain variation within NGC 3256. For the case of cosmic-ray or UV-induced photo-desorption, if it is increasing the abundances of methanol, it should be abundant in the two nuclei. The methanol abundances in the two nuclei are rather low. Therefore, if UV-photons or cosmic rays affect the methanol abundances, it is likely to decrease methanol abundances by photodissociation rather than to increase by photo-desorption. Therefore, we regard it most likely that methanol is enhanced by the shock due to the merger interaction or an outflow. Similar enhancement of methanol in the region of merger interaction was also reported by [Saito et al. \(2017\)](#) in VV114, a merger with a larger nuclear separation.

**HNC:** Observation in other galaxies show that the intensities of HNC vary in a similar way as  $\text{CH}_3\text{OH}$  when statistically analyzed position by position ([Meier & Turner 2005, 2012; Meier et al. 2015](#)). When seen in a large fractional abundance, the major formation route of HNC is likely from grain surface reaction ([Quan et al. 2010](#)) similarly to  $\text{CH}_3\text{OH}$ . In positions we analyze, positional variation of column densities of  $\text{CH}_3\text{OH}$  and HNC are similar to each other except for the N nucleus. A possible reason for the difference in the N nu-

cleus might be that HNC and  $\text{CH}_3\text{OH}$  abundances may act differently to the dust temperature. Methanol abundances decrease at high dust temperature because the hydrogen atom evaporate faster at the high dust temperatures, and the hydrogen atom is less likely to react (Acharyya & Herbst 2016). HNC may be able to sustain its abundance at higher dust temperatures than  $\text{CH}_3\text{OH}$  because there is less number of hydrogen necessary for HNC. This temperature dependence of HNC needs to be tested with chemical models. For the case of SiO column density ratios, there is a good correlation between HNC column density ratios. Such correlation between HNC and SiO was also proposed in Galactic high-mass star forming regions (Zinchenko et al. 2000). A survey of several galaxies by Martín et al. (2009) also suggested that a higher ratio of HNC is a characteristic for an early stage of starburst, dominated by shocks, instead of UV-photons.

**$\text{N}_2\text{H}^+$ :** In Galactic star-forming regions,  $\text{N}_2\text{H}^+$  emission is usually associated with dense cores (e.g., Storm et al. 2014; Pety et al. 2017). In our observations, column density ratios of  $\text{N}_2\text{H}^+$  over CS do not show clear variation, but the ratios over  $^{13}\text{CO}$  show a slightly higher value in the N nucleus than the S nucleus. It can be explained if the N nucleus contains more dense clouds than the S nucleus as argued in Section 3.2.

**$\text{HC}_3\text{N}$ :** In Galactic molecular clouds, higher abundances of cyanoacetylene ( $\text{HC}_3\text{N}$ ) are usually detected in dense cold clouds or hot protostellar cores. For extragalactic sources, it has been found that the compact obscured nuclei such as NGC 4418 and Arp 220 have high fractional abundance of  $\text{HC}_3\text{N}$  (Aalto et al. 2007; Costagliola & Aalto 2010; Martín et al. 2011; Lindberg et al. 2011). Since  $\text{HC}_3\text{N}$  is enhanced in star-forming regions, one can expect that  $\text{HC}_3\text{N}$  is more enhanced in regions of higher star formation efficiency. Although only the

N and S nuclei are known to have star formation (Lira et al. 2008) (and possibly a position TNE with a tentative detection of  $\text{H}40\alpha$  in this paper),  $N(\text{HC}_3\text{N})/N(^{13}\text{CO})$  is also enhanced in position C, a tidal arm with possible interaction with components.

**$\text{CH}_3\text{CCH}$ :** Propyne ( $\text{CH}_3\text{CCH}$ ) has been proposed as a diagnostics of starburst versus AGN by Aladro et al. (2015); starburst galaxies have high abundances of  $\text{CH}_3\text{CCH}$  while AGN-containing galaxies do not have detections of  $\text{CH}_3\text{CCH}$ . However, the reason behind this observational trend is still unknown. In NGC 3256, although the S nucleus is the likely AGN host,  $\text{CH}_3\text{CCH}$  column density ratios in the S nucleus are equivalent to or higher than in the N nucleus.

**$\text{HOC}^+$ :**  $\text{HOC}^+$  is a metastable isomer of  $\text{HCO}^+$ , and it needs irradiation from strong UV field (Goicoechea et al. 2017) or X-rays (Usero et al. 2004) to keep its abundance high. In NGC 3256, positions where  $\text{HOC}^+$  is enhanced are C and OS although the detection in OS is also tentative, and the error bars are large. The position OS contains the high-velocity gas coming from the outflow, and the position C also contains gas from the red-shifted outflow component (Figure 1 middle). The connection with the  $\text{HOC}^+$  abundance and the outflow can be suspected. However, the connection between the  $\text{HOC}^+$  enhancement and the outflow cannot be directly confirmed in the high-velocity gas alone because the high-velocity components are too weak to be detected for  $\text{HOC}^+$ .

**$\text{CCH}$ :** Ethynyl radical (CCH) is known to be enhanced in PDRs (e.g., Cuadrado et al. 2015), but there are also abundant in the early-time chemistry, and has been observed in the quiescent starless core such as TMC-1(CP) (Smith et al. 2004). Although CCH was also recently found in the outflow from an AGN in NGC 1068 (García-Burillo et al. 2017), its enhancement in the outflow is not seen in NGC

3256. This case is similar to NGC 1097, where no particular enhancement was seen around the AGN for CCH (Martín et al. 2015). Their abundances in NGC 3256 is highest in the N nucleus if the column density ratios over  $^{13}\text{CO}$ , but there is less variation among positions within NGC 3256 for ratios over CS.

#### 4.2. Comparison with other galactic nuclei

We next compare the chemistry in the nuclear positions in NGC 3256 and that of NGC 253 and Arp 220, galaxies with different star formation rates and efficiencies. The properties of these galaxies are summarized in Table 4.

NGC 253 is a well-studied, nearby starburst galaxy. The molecular gas distribution of the central molecular zone (CMZ) is similar to that of the Milky Way. However, the star formation rate inside is much higher than the Milky Way CMZ. Yet, NGC 3256 has even higher star formation rate within its CMZs. For NGC 253, we use the results by Aladro et al. (2015) taken by IRAM 30-meter telescope. The angular resolution of this IRAM study is  $17'' - 24''$ , which converts into  $300 - 400$  pc. This spatial scale is equivalent to the spatial resolution in our analysis of NGC 3256, which is  $\sim 300$  pc.

Like NGC 3256, Arp 220 is also a merger, but has even higher luminosity than NGC 3256. The nuclear separation of the two nuclei in Arp 220 is  $\sim 400$  pc on the sky, which is smaller than in the NGC3256. The column densities in Arp 220 are taken from results by Martín et al. (in preparation) where they used ALMA for the spectral scan of Bands 6 and 7 (see Martín et al. 2016, for some description of these data). The exact values of column densities and errors will be found in Martín et al. (in

preparation).<sup>6</sup> Their spatial resolution is also around 300 pc.

The column density ratios of the nuclei in NGC 253, NGC 3256, and Arp 220 are plotted in Figures 10 and 11, and these ratios are discussed below.

**HCN, HCO<sup>+</sup>, CS, and CN:** The column density ratios of HCN, HCO<sup>+</sup>, CS, and CN seem to follow similar trends; ratios are similar in NGC 3256(S & SW) and NGC 253, but values in NGC 3256(N), Arp 220 (E & W) are a factor of a few higher. Some exceptions are suppressed CN and HCO<sup>+</sup> by a factor of a few in Arp 220 compared with other species, and slightly enhanced CS in Arp 220 (W).

**SiO:** Among the galactic nuclei, Arp 220 has the highest column density ratios of SiO both over  $^{13}\text{CO}$  and CS. The spectral shapes observed in Arp 220 strongly suggests that it has molecular outflows from the both nuclei (Sakamoto et al. 2009) with the one from the western nucleus being more prominent (Sakamoto et al. 2017). It has been already discussed in Section 4.1 that the outflow from the N nucleus in NGC 3256 does not contribute to high SiO abundances. Unlike the outflow from the S nucleus in NGC 3256, each outflow in Arp 220 should be within the beam that covers each nucleus. These outflows might be the reason for the higher SiO abundances in Arp 220. An alternative explanation is that there are more cloud-cloud collisions in the dense and compact nuclei of Arp 220.

**CH<sub>3</sub>OH and HNCO:** Column density ratios of CH<sub>3</sub>OH and HNCO are lowest in the NGC

<sup>6</sup> We note that the analysis in Martín et al. (in preparation) did not use the Gaussian fit to the observed spectra for the calculation of column densities because they are severely affected by absorption at the line center. They use the side of the lines to calculate column densities. Therefore, we claim that the error of column densities from absorption is minimized, but it cannot be claimed that those values are free from absorption effects.

3256 nuclei than NGC 253 and Arp 220. As mentioned above, there are nuclear outflows in Arp 220, which can enhance the methanol and HNC abundance. At the same time, NGC 253 also has evidence of an outflow from the starburst (Sakamoto et al. 2006b; Bolatto et al. 2013). Alternatively, an enhancement in NGC 253 may be due to the cloud-cloud collision at the intersection of galactic orbits. Similar to SiO, the N nucleus of NGC 3256 does not seem to enhance  $\text{CH}_3\text{OH}$  and **HNC** by large amount.

**$\text{N}_2\text{H}^+$** : Although the column density ratios of  $N(\text{N}_2\text{H}^+)/N(^{13}\text{CO})$  have variation among the galactic nuclei, ratios  $N(\text{N}_2\text{H}^+)/N(\text{CS})$  have very little variation. This lack of variation may indicate that the column density ratios of  $N(\text{N}_2\text{H}^+)/N(^{13}\text{CO})$  may be the direct measure of dense cloud fraction, and that, within the dense gas,  $\text{N}_2\text{H}^+$  abundance does not vary much with respect to other molecules tracing the dense gas.

**$\text{HC}_3\text{N}$** : Here we can examine the relation of  $\text{HC}_3\text{N}$  fractional abundances and the star formation efficiency ( $= \tau_{\text{dep}}^{-1}$ , see Table 4). Although galactic nuclei with higher star formation efficiency tend to have higher  $\text{HC}_3\text{N}/^{13}\text{CO}$  ratios, variation among sources are not as large as the star formation efficiency itself (see also discussion in Section 5.3).

**$\text{CH}_3\text{CCH}$** : Column density ratios  $\text{CH}_3\text{CCH}/^{13}\text{CO}$  appear to be higher in sources with higher star formation efficiencies (see Section 5.3). However, as mentioned earlier, the behavior of this molecule is not well-known, and it is unclear what mechanism is causing the enhancement with higher star formation activity.

**$\text{HOC}^+$** : Ratios  $N(\text{HOC}^+)/N(^{13}\text{CO})$  is the highest in Arp220W, but there is little variation among the galactic nuclei for  $N(\text{HOC}^+)/N(\text{CS})$ . However, if  $N(\text{HOC}^+)/N(\text{HCO}^+)$  is plotted, it is also

the highest in Arp220W (Figure 12). Since  $N(\text{HOC}^+)/N(\text{HCO}^+)$  is more reliable because it is not affected by the difference of elemental abundance,  $\text{HOC}^+$  abundance in Arp 220W is likely higher than in other sources. Since Arp220W has a prominent outflow, the connection of  $\text{HOC}^+$  with outflows may be seen here again, but it needs to be confirmed with high-resolution imaging of Arp 220 in  $\text{HOC}^+$ . The effect of starburst in Arp 220 may also be the reason of increased  $N(\text{HOC}^+)/N(\text{HCO}^+)$ .

**CCH**: Since CCH is known to be a PDR tracer, one might expect higher fractional abundances of CCH in galaxies with higher star formation rates. However, this is not necessarily the case. A possible reason is the differences in the mean density. When the mean density in the ISM is very high, only a fraction of volume can be influenced by UV-photons because those photons become attenuated before reaching far from the vicinity of OB stars, and the enhancement of PDR tracers cannot be seen in a large scale.

#### 4.3. Comparison with a Galactic spiral arm region

Here we compare the chemical compositions of the tidal arm positions in our study with the one in W51 for relevant comparison among spiral arm positions. W51 is a molecular cloud complex in the Sagittarius arm in the Milky Way at the distance of 5.4 kpc (Sato et al. 2010). Within W51, there is an active star-forming region, which include a hot core W51 e1/e2. Watanabe et al. (2017) mapped various molecular species in  $\sim 40\text{ pc} \times 50\text{ pc}$  region in W51, and studied the average chemistry within this region so that their results can be compared with extragalactic interferometric observations taken with beam sizes of at least tens of parsecs. We do not discuss  $\text{HOC}^+$  here because this species was not detected in the averaged spectra of W51. Although their spatial scale is a factor of several smaller than our resolution,

we assume that there are molecular clouds with sizes similar to that of W51 within our beam, and compare the chemistry in the NGC 3256 arm positions and W51. Since [Watanabe et al. \(2017\)](#) only had data in the 3-mm band, they derived column densities using excitation temperatures of  $T_{\text{ex}} = 10, 15, 20$  K. Because the excitation temperatures of our results are  $T_{\text{ex}} = 10$  K or less, we use their column densities using  $T_{\text{ex}} = 10$  K. Although  $T_{\text{ex}}$  of some molecules are  $\sim 5$  K or so, we checked that the derived column densities do not vary significantly if we derive them by assuming  $T_{\text{ex}} = 10$  K for those molecules.

**HCN, HCO<sup>+</sup>, CS, and CN:** Molecules with higher critical densities have higher column densities ratios over <sup>13</sup>CO at the tidal arm positions in NGC 3256 than in W 51 (Figure 13). This trend may indicate the higher fraction of dense cloud in the beam in NGC 3256 tidal arms as discussed at the beginning of Section 4, where we suggest the variation of these ratios come from the variation of dense gas fraction within NGC 3256.

Column density ratios of other species are plotted in Figure 14.

**SiO:** The column density ratios of SiO both over <sup>13</sup>CO and CS at the position TSW are much higher than the upper limit in W51. This high abundance of SiO indicates more strong shocks in TSW of NGC 3256, possibly caused by the merger interaction. The upper limits at positions TNE and TSE are higher than that of W51, hence it is unknown whether these positions have more influence from shocks.

**CH<sub>3</sub>OH and HNCO:** Similarly to SiO, higher column density ratios of methanol and HNCO in NGC 3256 than in W51 are seen for ratios both over <sup>13</sup>CO and CS. Unlike SiO and HNCO, the enhancement is also seen in position TSE as well as in TSW for methanol.

**N<sub>2</sub>H<sup>+</sup>:** The trend of column density ratios of N<sub>2</sub>H<sup>+</sup> over <sup>13</sup>CO and CS is similar to that

of HC<sub>3</sub>N. The ratios over <sup>13</sup>CO are higher in NGC 3256 positions than that in W 51, but there is no obvious variation among positions for ratios over CS. Since N<sub>2</sub>H<sup>+</sup> is also abundant in more compact regions just like HC<sub>3</sub>N, the same explanation for HC<sub>3</sub>N can possibly used for this trend.

**HC<sub>3</sub>N:** Ratios  $N(\text{HC}_3\text{N})/N(^{13}\text{CO})$  are higher in the tidal arm positions in NGC 3256 than in W 51. However, the values of  $N(\text{HC}_3\text{N})/N(\text{CS})$  have very little variation among sources. In Galactic GMCs, HC<sub>3</sub>N comes from more compact regions than CS. If this is the case also in NGC 3256, our results indicate that within a CS-emitting cloud, there is a similar fraction of HC<sub>3</sub>N-emitting cores both in NGC 3256 and in W 51.

**CH<sub>3</sub>CCH:** In the tidal arm positions in NGC 3256,  $N(\text{CH}_3\text{CCH})/N(^{13}\text{CO})$  and  $N(\text{CH}_3\text{CCH})/N(\text{CS})$  are higher than in W 51. The ratio is the highest in TNE, the only off-nucleus position where H40 $\alpha$  was detected. A hint of positive correlation between the star formation rate and CH<sub>3</sub>CCH is again seen here, but the reason behind needs more investigation.

**CCH:** Ratios  $N(\text{CCH})/N(^{13}\text{CO})$  have higher values at the tidal arm position of NGC 3256 than in W 51, and  $N(\text{CCH})/N(\text{CS})$  does not vary much among those positions. This trend is similar to N<sub>2</sub>H<sup>+</sup> and HC<sub>3</sub>N. However, CCH having this similarity with N<sub>2</sub>H<sup>+</sup> and HC<sub>3</sub>N is puzzling because CCH is usually thought to come from rather extended regions.

## 5. DISCUSSION

### 5.1. <sup>13</sup>CO and C<sup>18</sup>O anomaly in LIRGs

It has been pointed out that the <sup>12</sup>CO/<sup>13</sup>CO and <sup>12</sup>C<sup>16</sup>O/C<sup>18</sup>O intensity ratios in luminous infrared galaxies are higher than in normal spiral galaxies ([Aalto et al. 1991](#); [Casoli et al. 1992](#)). [Casoli et al. \(1992\)](#) concluded that <sup>13</sup>CO and C<sup>18</sup>O lines are about four times weaker in NGC 3256 than what is normally expected



from  $^{12}\text{CO}$  in their single-dish observations. This variation in intensity ratios can be caused by excitation effects such as high temperature or turbulence (Aalto et al. 1991, 2010; Davis 2014). Turbulence can increase  $^{12}\text{CO}/^{13}\text{CO}$  by causing  $^{12}\text{CO}$  to be less optically thick, or turbulence occurs at the position where the low-metallicity gas inflows (Henkel et al. 2014; König et al. 2016). If this is the case, our chemistry analysis using column density ratios  $N(X)/N(^{13}\text{CO})$  is not affected.

However, it can also be caused by abundance deficit of  $^{13}\text{C}$  due to very young starburst or top-heavy initial mass function as proposed by Sliwa et al. (2017). The abundance ratio of  $^{12}\text{CO}/^{13}\text{CO}$  can also increase by the selective photo-desorption of  $^{13}\text{CO}$  because  $^{13}\text{CO}$  is less likely to be self-shielded. If it is caused by the elemental abundances of  $^{12}\text{C}/^{13}\text{C}$ , our derived column density ratios  $N(X)/N(^{13}\text{CO})$  may not reflect variation of only  $N(X)$ , but also of  $N(^{13}\text{CO})$ . If  $^{12}\text{CO}/^{13}\text{CO}$  column density ratios are higher in the tidal arm positions of NGC 3256 than in W 51, the higher ratios of  $N(X)/N(^{13}\text{CO})$  for most species in NGC 3256 shown in Figures 13 and 14 are due to variation of  $N(^{13}\text{CO})$ , and not  $N(X)$ . Further observations are needed to obtain the spatial dependence of  $^{12}\text{C}/^{13}\text{C}$ , and we leave it as future work.

### 5.2. Excitation or abundance?

From the variation of column density ratios of molecules with high critical densities over  $^{13}\text{CO}$ , we have argued that this variation should be a reflection of multiple components of different excitation conditions within the beam showing up as variation of apparent abundances. However, we cannot exclude the possibility that intrinsic variation of abundances is playing a role. The molecules we show in Figure 8, HCN,  $\text{HCO}^+$ , CS, and CN do have dependence on the temperature, the density, the UV or cosmic-ray ionization rate, but it is difficult to think that those

molecules all have similar variation among positions. Therefore, it is more likely that the density distribution function is the largest contributing factor of this variation.

### 5.3. Effects of starburst on the chemical composition

If some molecules emit only from compact star-forming regions, then the column densities of these molecules are proportional to the surface number density of the star-forming regions and hence should be proportional to the star formation rate in the observed area. For such molecules  $N(X)/N(^{13}\text{CO})$  should be proportional to the star formation efficiencies assuming that  $N(^{13}\text{CO}) \propto N(\text{H}_2)$ . Some column density ratios in Figure 11 are rearranged by the star formation efficiencies in Figure 15. As obviously seen in Figure 15, error bars on the star formation efficiencies are large due to uncertainty in molecular mass. Therefore, the precise relation cannot be determined, but there are some trends that can be discussed as below. Although  $\text{HC}_3\text{N}$  and  $\text{N}_2\text{H}^+$  are molecules found preferentially in denser regions, those molecules do not have strong correlation with the star formation efficiency when compared among different galactic nuclei. NGC 3256 has at least a factor of a few, but more likely about an order of magnitude, star formation efficiency than NGC 253, while Arp 220 and NGC 3256 have similar star formation efficiencies. The differences of  $N(\text{HC}_3\text{N})/N(^{13}\text{CO})$  and  $N(\text{N}_2\text{H}^+)/N(^{13}\text{CO})$  among the three galactic nuclei are not as large as the variation of star formation efficiency.

There are a few possible reasons for this lack of correlation between the abundances of those molecules and the star formation efficiencies. First, those molecules may not be tracing the star-forming regions. For example,  $\text{HC}_3\text{N}$  may also be enhanced in shocks (e.g., Harada et al. 2015). Another explanation is that  $\text{HC}_3\text{N}$  is prone to dissociation by UV-photons, and may decrease in abundances in PDRs.  $\text{N}_2\text{H}^+$  abun-

dances may also be influenced by the cosmic-ray ionization rate. Second, molecular clouds may already be reflecting the next time step of star formation because those clouds are places of future star formation. If the feedback from the existing stars is suppressing the on-going star formation, the chemistry is unlikely to reflect the star formation rate. However, it is hard to assume that NGC 3256 is already quenching star formation before the final stage of the merging event.

The column density ratios  $N(\text{CH}_3\text{CCH})/N(^{13}\text{CO})$  do seem to vary as the star formation efficiency, but the behavior of this molecule still needs to be understood.

#### 5.4. *Effects of a merging event on the properties of the ISM*

From our observations of SiO and  $\text{CH}_3\text{OH}$ , it is likely that frequent shocks are occurring in tidal arms of NGC 3256. Such shocked ISM is also proposed to be present galaxy-wide in NGC 3256 from observations of optical emission lines by Rich et al. (2011), and they suggested shocks as important mechanism to dissipate kinetic energy and angular momentum, which can promote the transport of gas into the central regions. Our observations also suggest higher fraction of dense clouds in the tidal arms of NGC 3256 than in W 51, likely due to the compression from the shock. If such compression occurs, one could ask a question whether this compression can induce star formation by cloud-cloud collision. Judging from the IR observations and the radio recombination line in our observations, there is no such evidence of enhancement. In fact, positions with high abundance of shock molecular tracers such as TSE or TSW are the positions that lack the evidence of star formation.

## 6. SUMMARY

We have conducted a molecular line survey using ALMA Band 3 and Band 6 in an infrared-

luminous merger NGC 3256. This paper first presents continuum images, velocity-integrated intensity maps, and intensity ratio maps. From the observed intensities, column densities of detected molecules are derived in 8 positions of interest including the two nuclei, tidal arms positions, and outflow positions. We have compared the derived molecular compositions within NGC 3256, among some galactic nuclei in NGC 3256, Arp 220, and NGC 253, and between the tidal arms of NGC 3256 and a spiral arm in our Galaxy at W 51.

Here are our main findings:

- The intensity ratios of  $\text{HCN}(1-0)/\text{HCO}^+(1-0)$  and  $\text{HCN}(1-0)/\text{CS}(2-1)$  are lower in the S nucleus than in the N nucleus. The S nucleus has some signs of an AGN while the N nucleus does not have any evidence of an AGN. Previous statistical studies of  $\text{HCN}/\text{HCO}^+$  and  $\text{HCN}/\text{CS}$  in other galaxies showed enhanced ratios in AGN-containing galaxies (Kohno et al. 2001; Imanishi & Nakanishi 2014; Izumi et al. 2016), and our results in NGC 3256 do not follow this trend.
- Higher influence of shock is found in the outflow position from the southern galaxy of NGC 3256 shown in SiO observations.
- Comparing the chemistry of NGC 3256, NGC 253, and Arp 220, Arp 220 shows an enhancement in  $N(\text{HC}_3\text{N})/N(^{13}\text{CO})$  and  $N(\text{SiO})/N(^{13}\text{CO})$ . The enhancement of  $\text{HC}_3\text{N}$  is likely to be caused by the hot and dense ISM of Arp 220, while SiO abundances may be increased due to the shock from the outflows.
- We examined the relationship with the column density ratios over  $^{13}\text{CO}$  of observed species among the galactic nuclei of NGC 3256, NGC 253, and Arp 220. The only ratio that seems to positively correlate with the star formation efficiency

is  $N(\text{CH}_3\text{CCH})/N(^{13}\text{CO})$ , which needs more understanding of major formation and destruction routes.

- The tidal arm positions in NGC 3256 also have strong influence of shock compared with Galactic spiral arm position. They also show hints of compression due to higher apparent column density ratios of molecules with higher critical densities over  $^{13}\text{CO}$ , but these ratios may also be due to lower  $^{13}\text{C}$  elemental abundances.

Our line survey in two frequency bands has highlighted the chemical and physical variation of the ISM within NGC 3256 and among galaxies. Further analysis of the physical conditions such as the temperature and the density using the large velocity gradient analysis would help our understanding of the chemistry. The physics and the chemistry of outflow features are worth future follow-up studies.

We are extremely grateful to the ALMA staff for their service in observations, quality

assessment, and local assistance at Taiwanese ALMA regional center (ARC). This paper makes use of the following ALMA data: ADS/JAO.ALMA#2015.1.00412.S, ADS/JAO.ALMA#2016.1.00965.S, ADS/JAO.ALMA#2015.1.00993.S, and ADS/JAO.ALMA#2011.0.00525.S. ALMA is a partnership of ESO (representing its member states), NSF (USA) and NINS (Japan), together with NRC (Canada), MOST and ASIAA (Taiwan), and KASI (Republic of Korea), in cooperation with the Republic of Chile. The Joint ALMA Observatory is operated by ESO, AUI/NRAO and NAOJ. KSA and NH were supported by the grant MOST 106-2119-M-001-025 from the Ministry of Science and Technology, Taiwan.

*Facilities:* ALMA

*Software:* CASA (*v4.5.3*, *v4.6*, and *v4.7* [McMullin et al. 2007](http://casac.nrao.edu)), MADCUBA (<http://cab.inta-csic.es/madcuba/Portada.html>)

## REFERENCES

- Aalto, S., Beswick, R., & Jütte, E. 2010, *A&A*, 522, A59
- Aalto, S., Garcia-Burillo, S., Muller, S., Winters, J. M., van der Werf, P., Henkel, C., Costagliola, F., & Neri, R. 2012, *A&A*, 537, A44
- Aalto, S., Johansson, L. E. B., Booth, R. S., & Black, J. H. 1991, *A&A*, 249, 323
- Aalto, S., Monje, R., & Martín, S. 2007, *A&A*, 475, 479
- Aalto, S., Polatidis, A. G., Hüttemeister, S., & Curran, S. J. 2002, *A&A*, 381, 783
- Aalto, S., et al. 2015a, *A&A*, 574, A85
- . 2015b, *A&A*, 584, A42
- Acharyya, K., & Herbst, E. 2016, *ApJ*, 822, 105
- Aladro, R., et al. 2015, *A&A*, 579, A101
- Amo-Baladrón, M. A., Martín-Pintado, J., Morris, M. R., Muno, M. P., & Rodríguez-Fernández, N. J. 2009, *ApJ*, 694, 943
- Ando, R., et al. 2017, *ApJ*, 849, 81
- Barcos-Muñoz, L., et al. 2015, *ApJ*, 799, 10
- Bolatto, A. D., et al. 2013, *Nature*, 499, 450
- Casoli, F., Dupraz, C., & Combes, F. 1992, *A&A*, 264, 49
- Costagliola, F., & Aalto, S. 2010, *A&A*, 515, A71
- Costagliola, F., et al. 2015, *A&A*, 582, A91
- Cuadrado, S., Goicoechea, J. R., Pilleri, P., Cernicharo, J., Fuente, A., & Joblin, C. 2015, *A&A*, 575, A82
- Davis, T. A. 2014, *MNRAS*, 445, 2378
- D’Onghia, E., Vogelsberger, M., Faucher-Giguere, C.-A., & Hernquist, L. 2010, *ApJ*, 725, 353
- Emonts, B. H. C., Piqueras-López, J., Colina, L., Arribas, S., Villar-Martín, M., Pereira-Santaella, M., Garcia-Burillo, S., & Alonso-Herrero, A. 2014, *A&A*, 572, A40
- García-Burillo, S., et al. 2014, *A&A*, 567, A125
- . 2017, *A&A*, 608, A56
- Goicoechea, J. R., et al. 2017, *A&A*, 601, L9

- Gusdorf, A., Cabrit, S., Flower, D. R., & Pineau Des Forêts, G. 2008, *A&A*, 482, 809
- Haan, S., et al. 2011, *AJ*, 141, 100
- Harada, N. 2017, in *IAU Symposium*, Vol. 332, *Astrochemistry VII - Through the Cosmos from Galaxies to Planets*, ed. M. Cunningham, T. J. Millar, & Y. Aikawa, in press
- Harada, N., Herbst, E., & Wakelam, V. 2010, *ApJ*, 721, 1570
- Harada, N., et al. 2015, *A&A*, 584, A102
- Henkel, C., et al. 2014, *A&A*, 565, A3
- Imanishi, M., & Nakanishi, K. 2014, *AJ*, 148, 9
- Izumi, T., et al. 2016, *ApJ*, 818, 42
- Kauffmann, J., Goldsmith, P. F., Melnick, G., Tolls, V., Guzman, A., & Menten, K. M. 2017, *A&A*, 605, L5
- Kohno, K., Matsushita, S., Vila-Vilaró, B., Okumura, S. K., Shibatsuka, T., Okiura, M., Ishizuki, S., & Kawabe, R. 2001, in *Astronomical Society of the Pacific Conference Series*, Vol. 249, *The Central Kiloparsec of Starbursts and AGN: The La Palma Connection*, ed. J. H. Knapen, J. E. Beckman, I. Shlosman, & T. J. Mahoney, 672
- König, S., Aalto, S., Muller, S., Gallagher, J. S., Beswick, R. J., Xu, C. K., & Evans, A. 2016, *A&A*, 594, A70
- Leitherer, C., Chandar, R., Tremonti, C. A., Wofford, A., & Schaerer, D. 2013, *ApJ*, 772, 120
- Leroy, A. K., et al. 2015, *ApJ*, 801, 25
- Lindberg, J. E., Aalto, S., Costagliola, F., Pérez-Beaupuits, J.-P., Monje, R., & Muller, S. 2011, *A&A*, 527, A150
- Lira, P., Gonzalez-Corvalan, V., Ward, M., & Hoyer, S. 2008, *MNRAS*, 384, 316
- Lira, P., Ward, M., Zezas, A., Alonso-Herrero, A., & Ueno, S. 2002, *MNRAS*, 330, 259
- Loenen, A. F., Spaans, M., Baan, W. A., & Meijerink, R. 2008, *A&A*, 488, L5
- Martín, S., Martín-Pintado, J., & Mauersberger, R. 2009, *ApJ*, 694, 610
- Martín, S., et al. 2011, *A&A*, 527, A36
- . 2015, *A&A*, 573, A116
- . 2016, *A&A*, 590, A25
- McMullin, J. P., Waters, B., Schiebel, D., Young, W., & Golap, K. 2007, in *Astronomical Society of the Pacific Conference Series*, Vol. 376, *Astronomical Data Analysis Software and Systems XVI*, ed. R. A. Shaw, F. Hill, & D. J. Bell, 127
- Meier, D. S., & Turner, J. L. 2005, *ApJ*, 618, 259
- . 2012, *ApJ*, 755, 104
- Meier, D. S., et al. 2015, *ApJ*, 801, 63
- Nakajima, T., et al. 2015, *PASJ*, 67, 8
- Neff, S. G., Ulvestad, J. S., & Campion, S. D. 2003, *ApJ*, 599, 1043
- Nishimura, Y., Watanabe, Y., Harada, N., Shimonishi, T., Sakai, N., Aikawa, Y., Kawamura, A., & Yamamoto, S. 2017, *ApJ*, 848, 17
- Ohyama, Y., Terashima, Y., & Sakamoto, K. 2015, *ApJ*, 805, 162
- Pety, J., et al. 2017, *A&A*, 599, A98
- Privon, G. C., et al. 2017, *ApJ*, 835, 213
- Quan, D., Herbst, E., Osamura, Y., & Roueff, E. 2010, *ApJ*, 725, 2101
- Rich, J. A., Kewley, L. J., & Dopita, M. A. 2011, *ApJ*, 734, 87
- Saito, T., et al. 2017, *ApJ*, 834, 6
- Sakamoto, K., Aalto, S., Combes, F., Evans, A., & Peck, A. 2014, *ApJ*, 797, 90
- Sakamoto, K., Aalto, S., Evans, A. S., Wiedner, M. C., & Wilner, D. J. 2010, *ApJL*, 725, L228
- Sakamoto, K., Ho, P. T. P., & Peck, A. B. 2006a, *ApJ*, 644, 862
- Sakamoto, K., et al. 2006b, *ApJ*, 636, 685
- . 2009, *ApJL*, 700, L104
- . 2017, *ApJ*, 849, 14
- Sanders, D. B., Mazzarella, J. M., Kim, D.-C., Surace, J. A., & Soifer, B. T. 2003, *AJ*, 126, 1607
- Sato, M., Reid, M. J., Brunthaler, A., & Menten, K. M. 2010, *ApJ*, 720, 1055
- Schöier, F. L., van der Tak, F. F. S., van Dishoeck, E. F., & Black, J. H. 2005, *A&A*, 432, 369
- Shirley, Y. L. 2015, *PASP*, 127, 299
- Sliwa, K., Wilson, C. D., Aalto, S., & Privon, G. C. 2017, *ApJL*, 840, L11
- Smith, I. W. M., Herbst, E., & Chang, Q. 2004, *MNRAS*, 350, 323
- Sorai, K., Nakai, N., Kuno, N., Nishiyama, K., & Hasegawa, T. 2000, *PASJ*, 52, 785
- Stierwalt, S., et al. 2013, *ApJS*, 206, 1
- Storm, S., et al. 2014, *ApJ*, 794, 165
- Takano, S., et al. 2014, *PASJ*, 66, 75
- Tully, R. B., et al. 2013, *AJ*, 146, 86
- Usero, A., García-Burillo, S., Fuente, A., Martín-Pintado, J., & Rodríguez-Fernández, N. J. 2004, *A&A*, 419, 897
- Viti, S., et al. 2014, *A&A*, 570, A28

- Watanabe, Y., Nishimura, Y., Harada, N., Sakai, N., Shimonishi, T., Aikawa, Y., Kawamura, A., & Yamamoto, S. 2017, ApJ, 845, 116
- Zinchenko, I., Henkel, C., & Mao, R. Q. 2000, A&A, 361, 1079



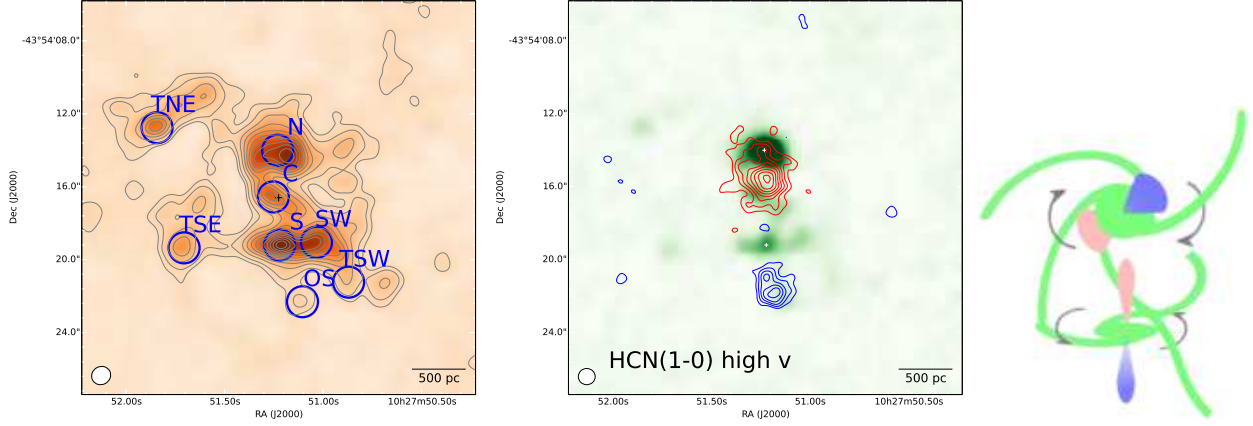


**Figure 1.** (Left) Eight positions analyzed in the Section 4 are shown on the velocity-integrated intensity map of  $^{13}\text{CO}$  (2 – 1). (Middle) Positions of components in HCN (1 – 0) with large velocity shifts from the systemic velocity are shown in red contours for the velocity range +225 to +375  $\text{km s}^{-1}$ , and blue contours for the velocity range -435 to -195  $\text{km s}^{-1}$  relative to the systemic velocity. Contour levels are starting from  $3\sigma$  for every  $1\sigma$ . (Right) A schematic image of the merger system of NGC 3256 reproduced from a similar image in Sakamoto et al. (2014). Two nuclear disks, spiral arms, and outflows from both galaxies are shown.

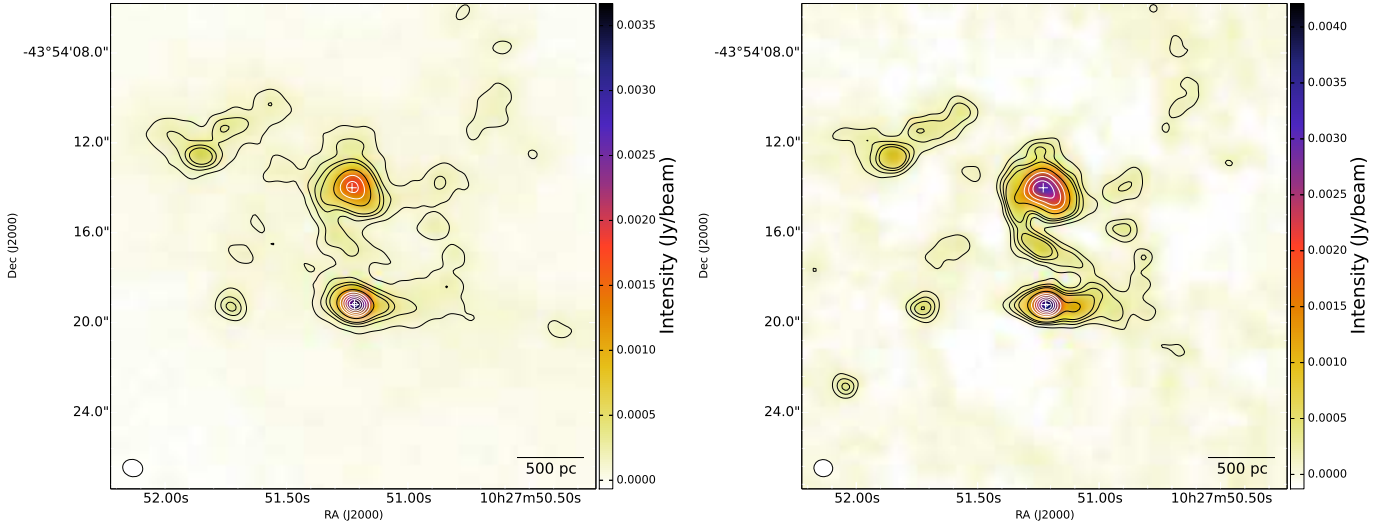


**Figure 2.** Continuum maps at (left)  $\lambda = 3.0$  mm and (right)  $\lambda = 1.2$  mm. Contour levels are (left)  $5\sigma$ ,  $10\sigma$ ,  $15\sigma$ ,  $20\sigma$ , and every  $20\sigma$  afterwards where  $1\sigma = 0.022$  mJy, and  $3\sigma$ ,  $6\sigma$ ,  $9\sigma$ ,  $12\sigma$ , and every  $12\sigma$  afterwards where  $1\sigma = 0.043$  mJy.

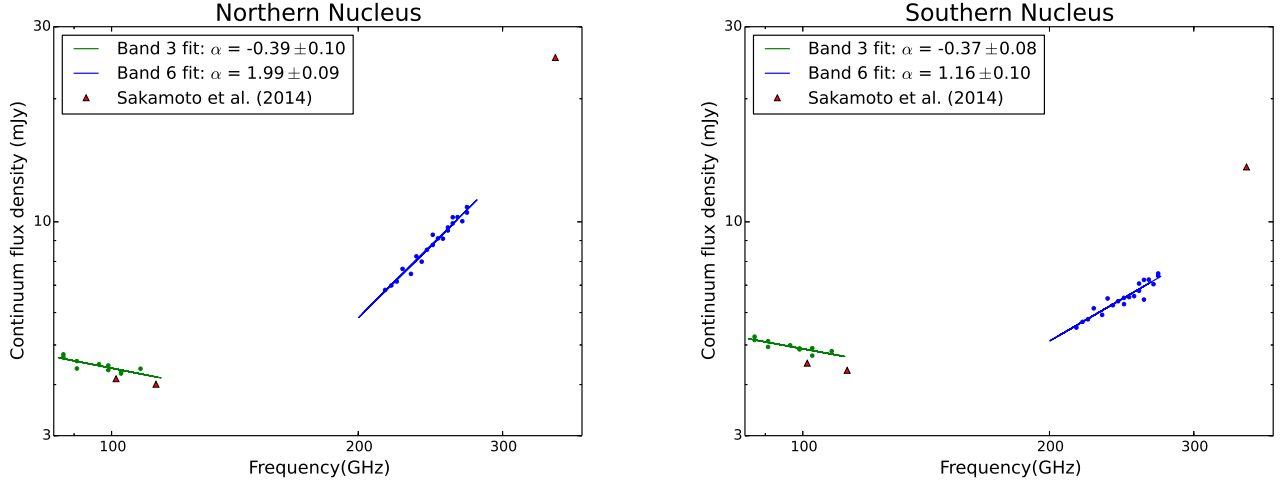


**Figure 3.** Continuum flux densities within  $2.0''$  from the radio peaks of (left:) the northern nucleus and (right:) the southern nucleus as a function of frequency from our observations in the log scale on both axes. Solid line show fits of spectral index for Bands 3 and 6. Values from Cycle 0 by [Sakamoto et al. \(2014\)](#) are also plotted as a reference with red triangles. The value in Band 7 from the Cycle 0 observation was taken by using both sidebands.

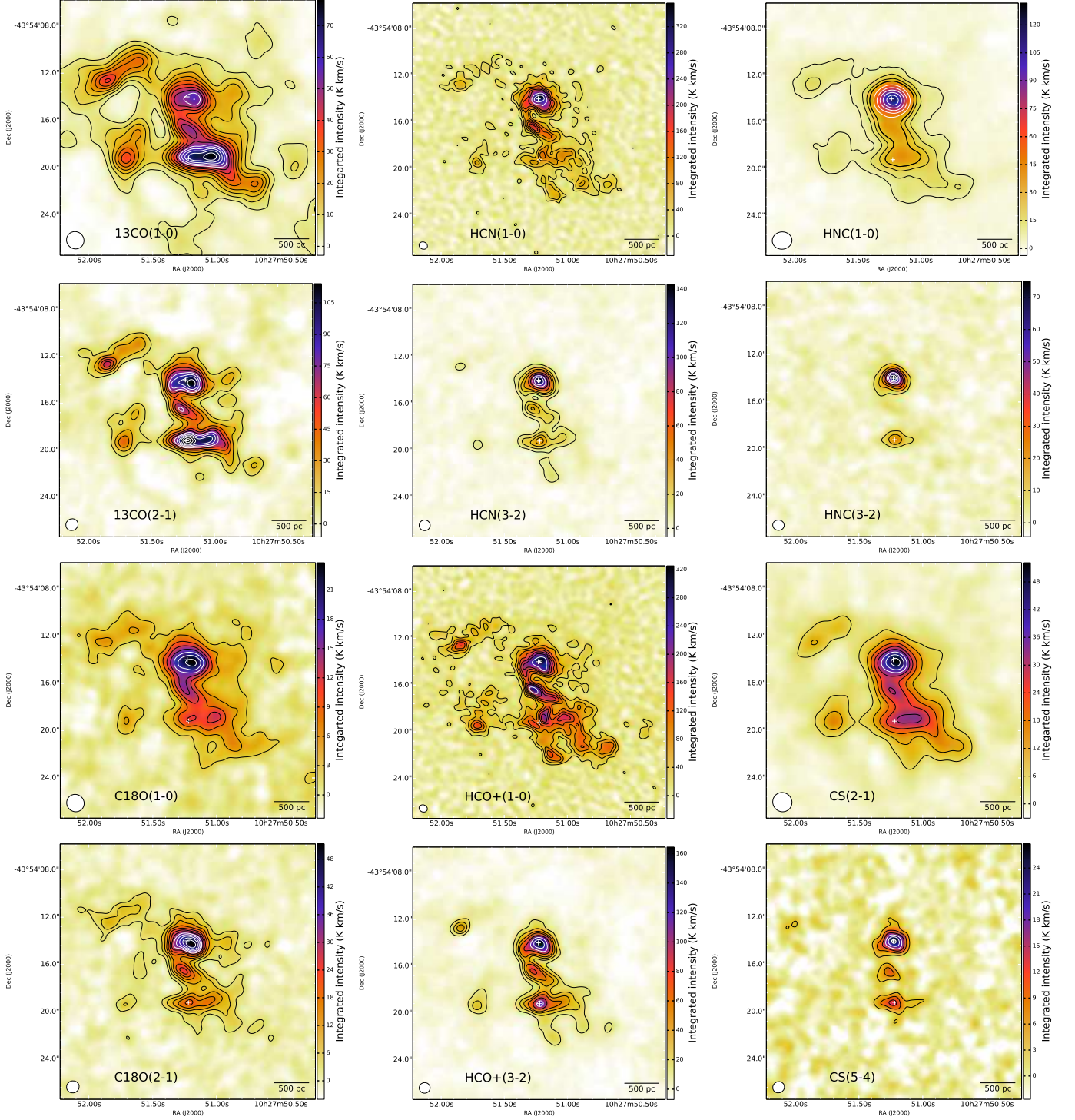


**Figure 4.** Velocity-integrated intensity maps of selected observed lines. Contour levels are every  $6\sigma$  for  $^{13}\text{CO}$  (1-0),  $^{13}\text{CO}$  (2-1), HCN(3-2), every  $3\sigma$  for HCN(1-0),  $\text{C}^{18}\text{O}$ (1-0),  $\text{C}^{18}\text{O}$ (2-1),  $\text{HCO}^+$ (1-0), CS(5-4),  $6\sigma$ ,  $12\sigma$ ,  $18\sigma$ ,  $24\sigma$ , and every  $12\sigma$  for HCN(3-2),  $\text{HCO}^+$ (3-2), and HNC(1-0). The rms values are listed in Table 2.



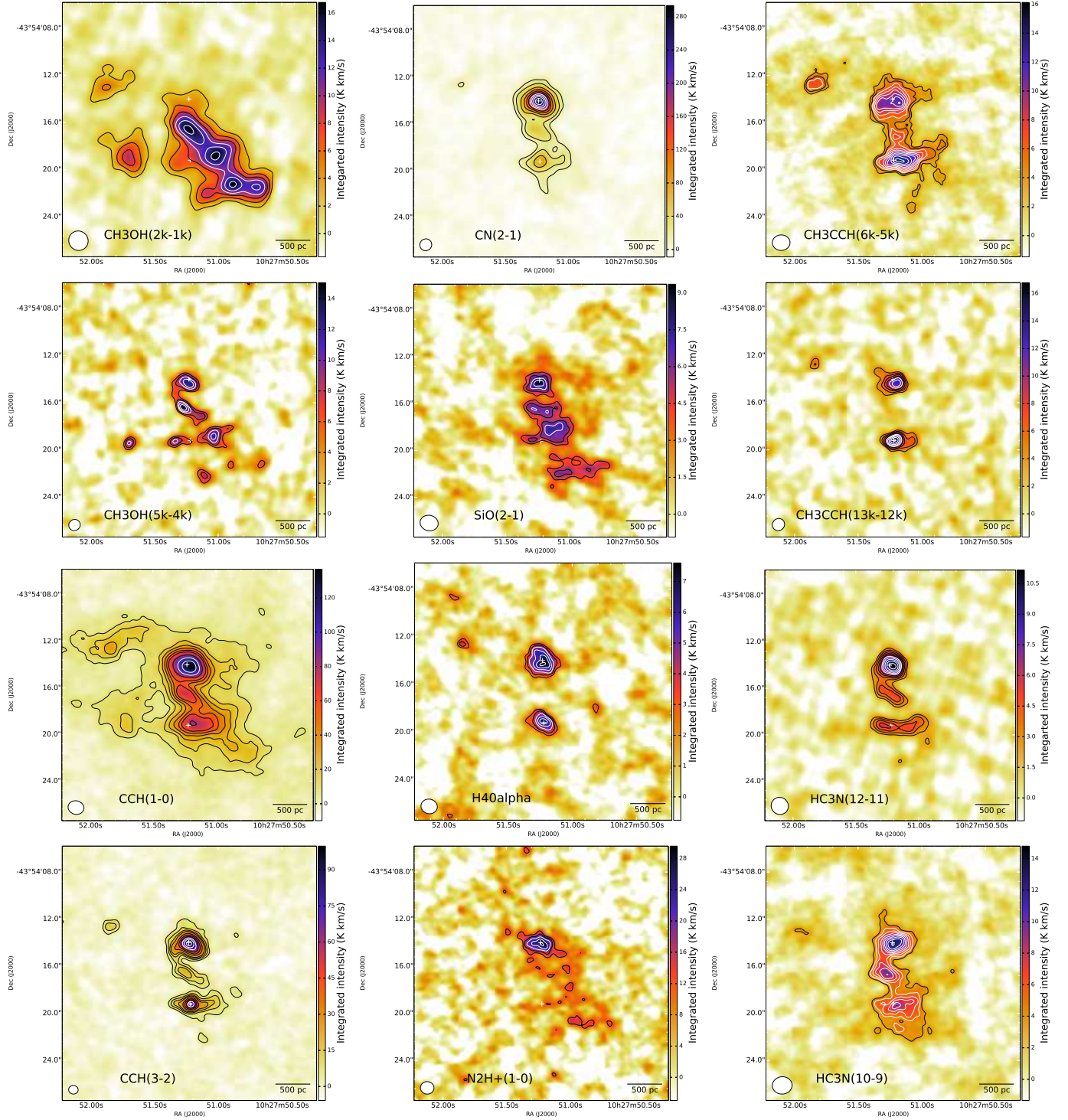


**Figure 5.** Same as Figure 4, but for other transitions. Contour levels are chosen as every  $3\sigma$  for  $\text{CH}_3\text{OH}(2_k - 1_k)$ ,  $\text{CCH}(1-0)$ , every  $1\sigma$  starting from  $3\sigma$  for  $\text{CH}_3\text{OH}(5_k - 4_k)$ ,  $\text{SiO}(2-1)$ ,  $\text{H40}\alpha$ ,  $\text{N}_2\text{H}^+(1-0)$ ,  $\text{CH}_3\text{CCH}(6_k - 5_k)$ ,  $\text{CH}_3\text{CCH}(13_k - 12_k)$ ,  $\text{HC}_3\text{N}(12-11)$ ,  $\text{HC}_3\text{N}(10-9)$ , and every  $5\sigma$  for  $\text{CN}(2-1)$ , and  $3\sigma$ ,  $6\sigma$ ,  $9\sigma$ ,  $12\sigma$ , and every  $6\sigma$  for  $\text{CCH}(2-1)$ . For CCH and CN, we integrated the velocity ranges to include all the doublets / triplets. The rms values are listed in Table 2.

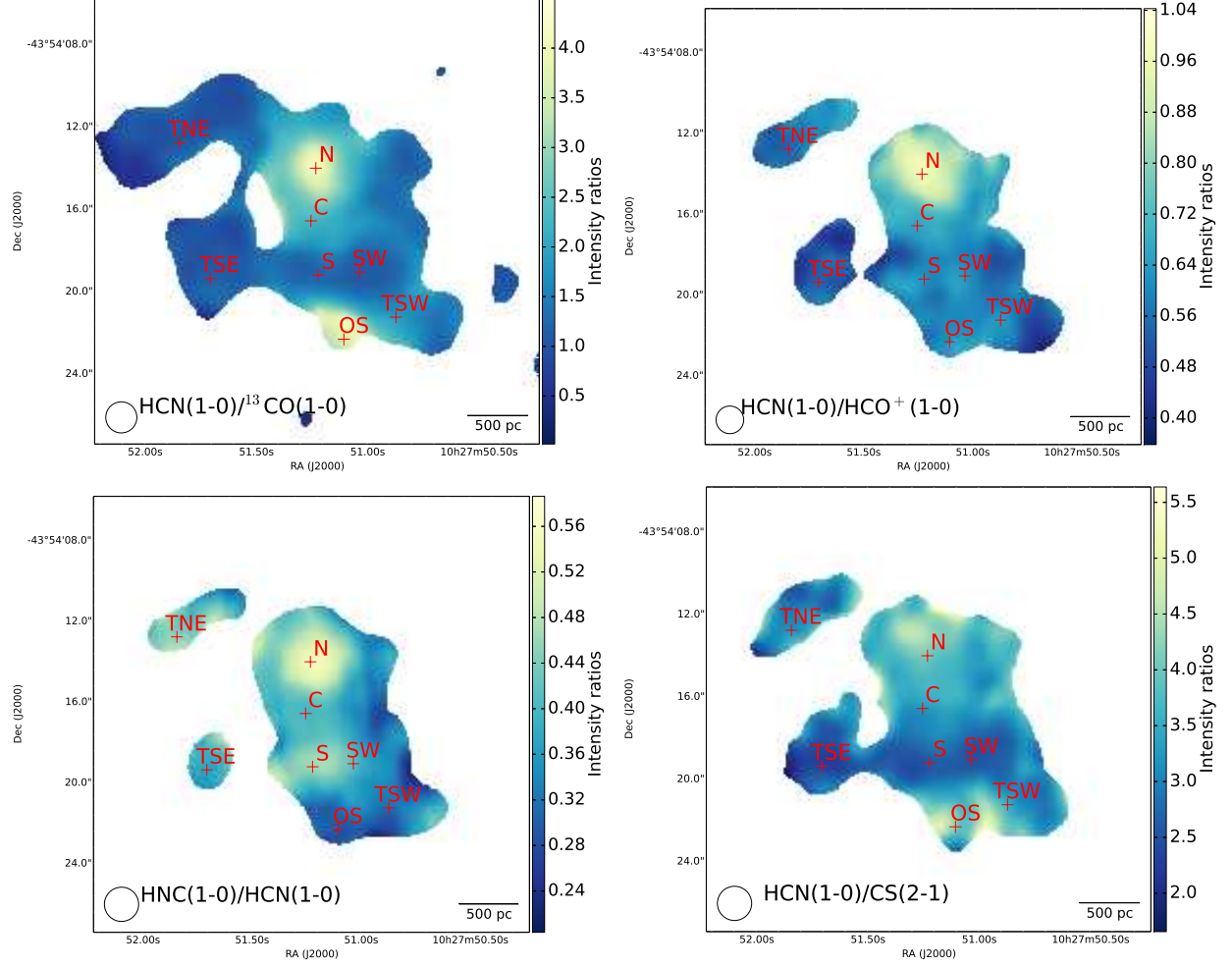


**Figure 6.** Maps of intensity ratios of (upper left)  $\text{HCN}(1-0)/^{13}\text{CO}(1-0)$ , (upper right)  $\text{HCN}(1-0)/\text{HCO}^+(1-0)$ , (lower left)  $\text{HNC}(1-0)/\text{HCN}(1-0)$ , and (lower right)  $\text{HCN}(1-0)/\text{CS}(2-1)$ . The ratios are calculated for the intensity units in Kelvin scale. Positions shown in Figure 1 are marked with red crosses.



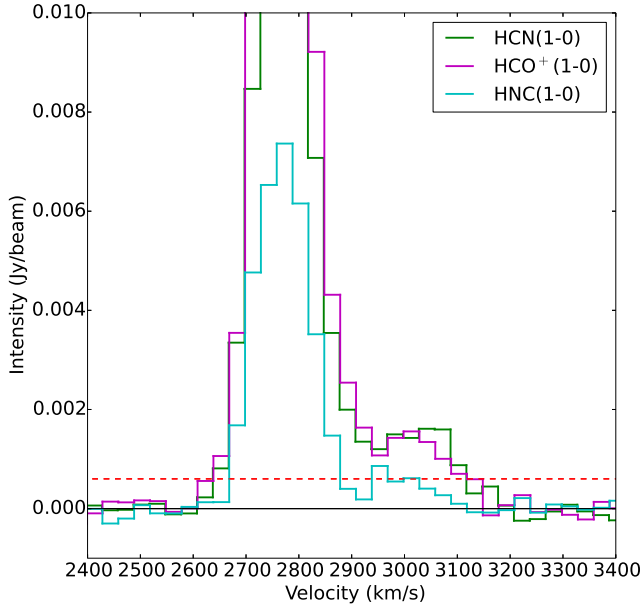


**Figure 7.** Spectra of  $\text{HCN}(1-0)$ ,  $\text{HCO}^+(1-0)$ , and  $\text{HNC}(1-0)$  at the peak of red-shifted outflow components shown in Figure 1 (*middle*) are plotted with green, magenta, and cyan, respectively. Spectra are extracted from cubes convolved to  $1.7''$ . The value of  $3\sigma$  is plotted with a red dotted line. The systemic velocity is  $2775 \text{ km s}^{-1}$ , and the emission from  $v > 2975 \text{ km s}^{-1}$  is likely to come from the outflow.

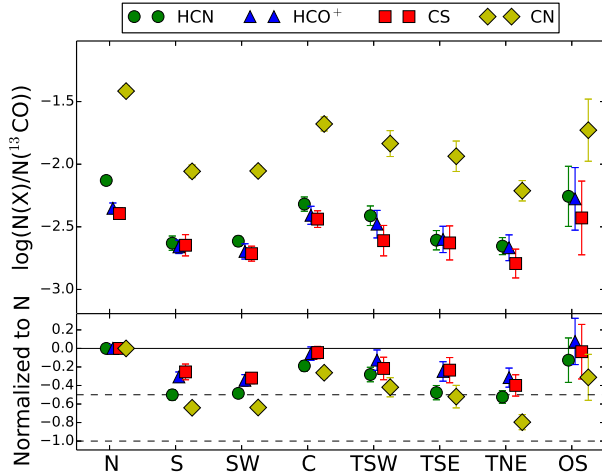


**Figure 8.** (*Top*) Column density ratios of  $\text{HCN}$ ,  $\text{HCO}^+$ ,  $\text{CS}$ , and  $\text{CN}$  over  $^{13}\text{CO}$  at positions N, S, C, TNE, TSE, TSW, OS, and SW in NGC 3256. Errors of individual column densities are automatically calculated from the Gaussian fitting by MADCUBA. (*Bottom*) The same figure as the top figure, but all the values are normalized to the position “N”. All the values are shown in a log scale.

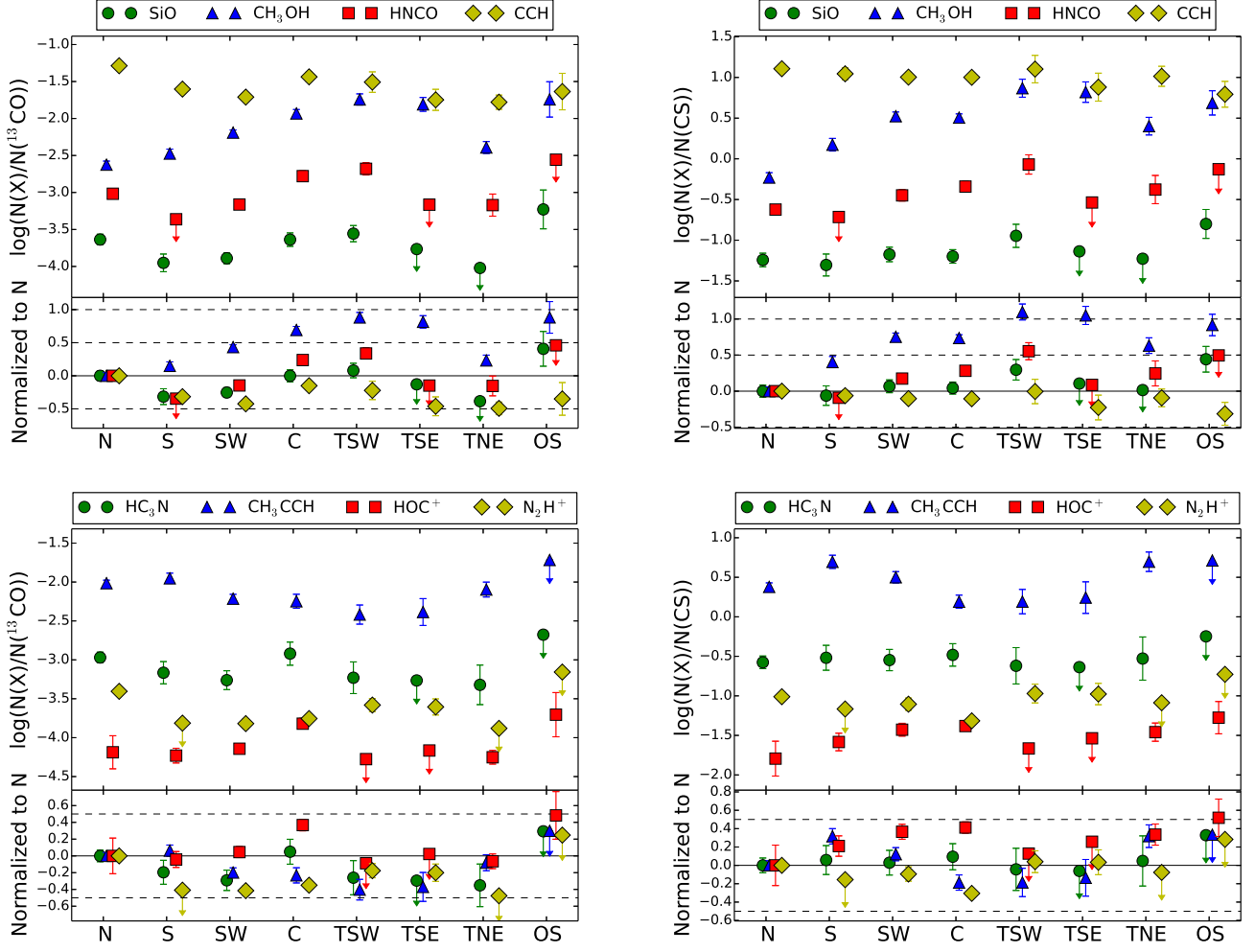


**Figure 9.** (Top) Column density ratios of selected species over  $^{13}\text{CO}$  (left panels) and over CS (right panels) at positions N, S, C, TNE, TSE, TSW, OS, and SW in NGC 3256. (Bottom) The same figure as the top figure, but all the values are normalized to the position “N”. All the values are shown in a log scale.

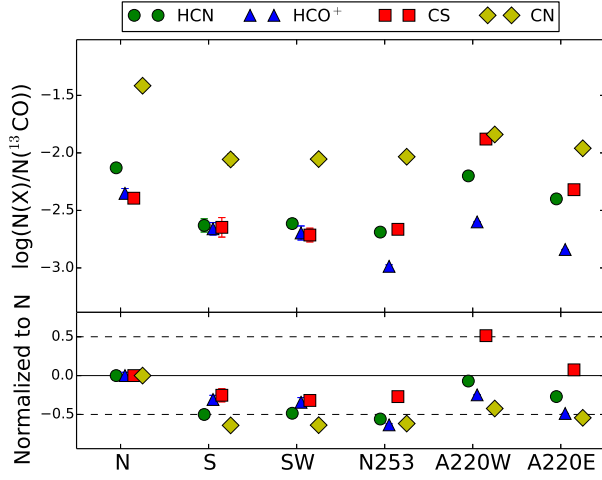


**Figure 10.** (*Top*) Column density ratios of HCN, HCO<sup>+</sup>, CS, and CN over <sup>13</sup>CO and over CS at nuclear positions N, S, and SW in NGC 3256, in NGC 253, and W and E in Arp 220. (*Bottom*) The same figure as the top figure, but all the values are normalized to the position “N”. All the values are shown in a log scale.

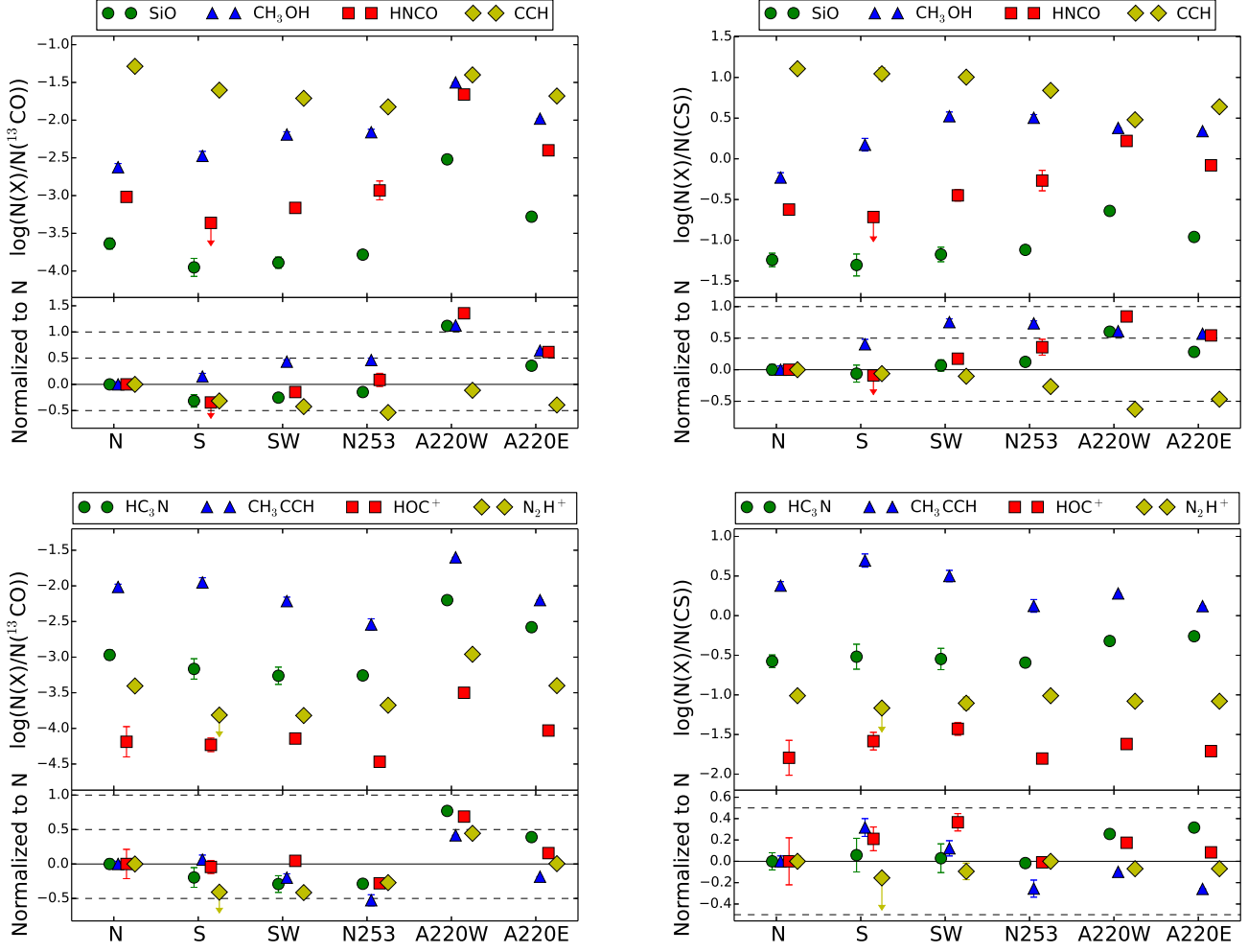


**Figure 11.** (*Top*) Column density ratios of selected species over  $^{13}\text{CO}$  (left panels) and over CS (right panels) at nuclear positions N, S, and SW in NGC 3256, in NGC 253, and W and E in Arp 220. (*Bottom*) The same figure as the top figure, but all the values are normalized to the position “N”. All the values are shown in a log scale.

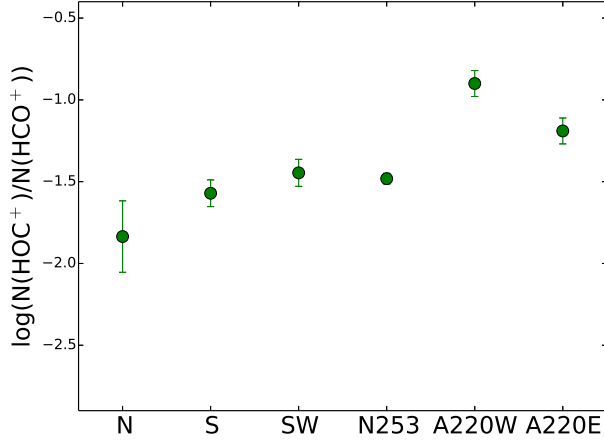


**Figure 12.** Column density ratios of  $\text{HOC}^+$  over  $\text{HCO}^+$  at nuclear positions N, S, and SW in NGC 3256, in NGC 253, and W and E in Arp 220.

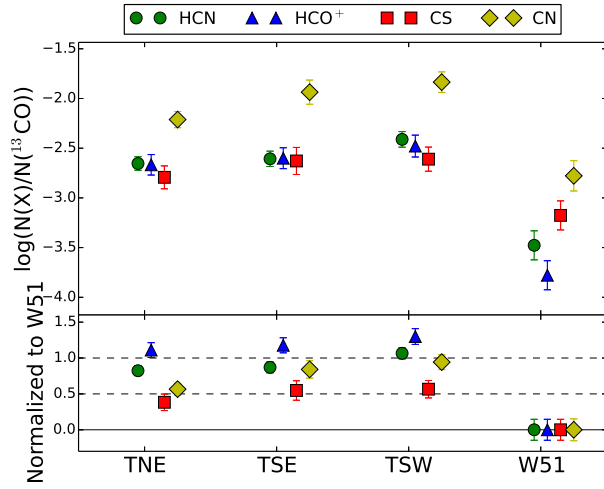


**Figure 13.** (*Top*) Column density ratios of HCN,  $\text{HCO}^+$ , CS, and CN over  $^{13}\text{CO}$  at tidal arm positions in NGC 3256 (TNE, TSE, and TSW) and W51. (*Bottom*) The same figure as the top figure, but all the values are normalized to W51. All the values are shown in a log scale.



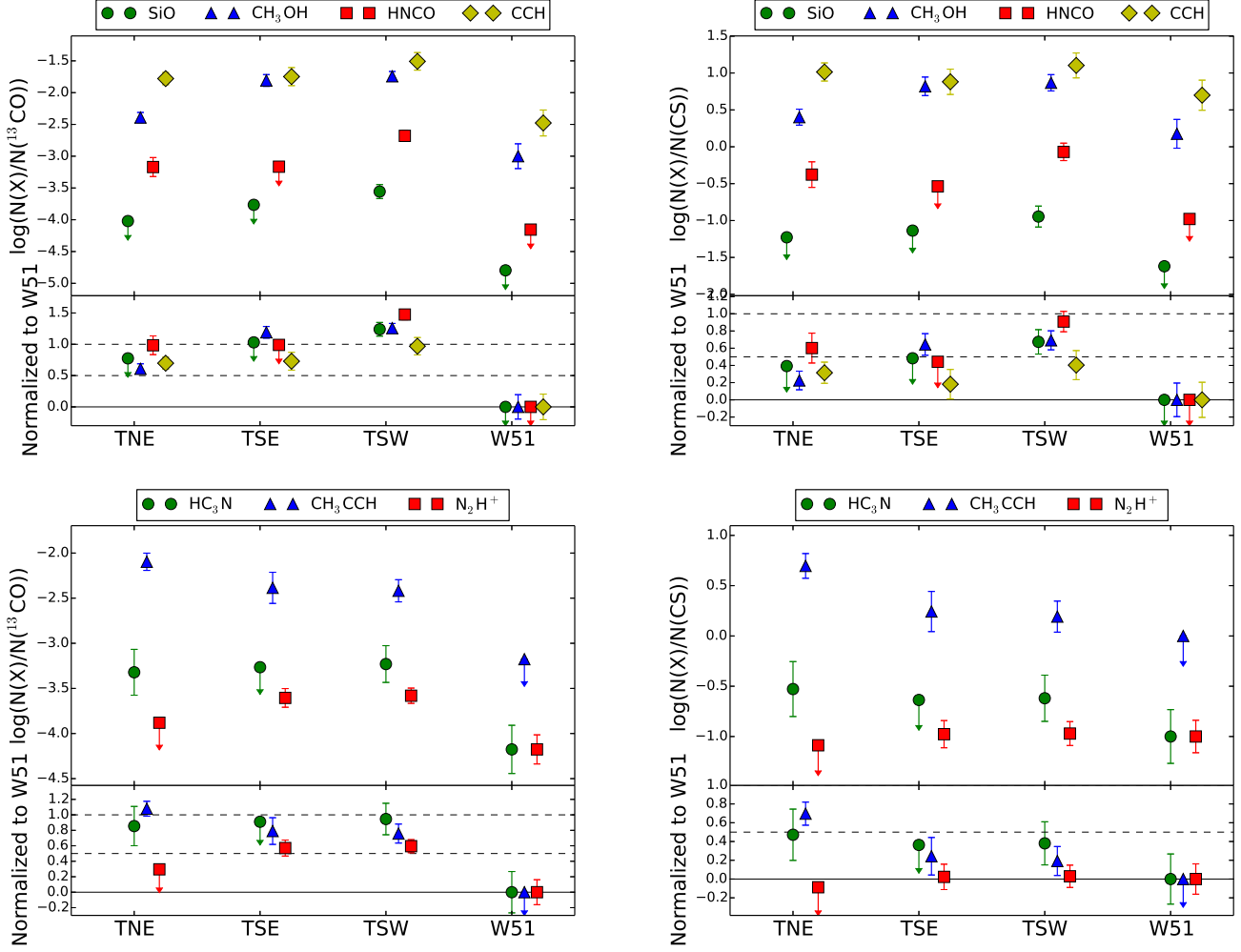


**Figure 14.** (*Top*) Column density ratios of selected species over  $^{13}\text{CO}$  (left panels) and over CS (right panels) at tidal arm positions in NGC 3256 (TNE, TSE, and TSW) and W51. (*Bottom*) The same figure as the top figure, but all the values are normalized to W51. All the values are shown in a log scale.

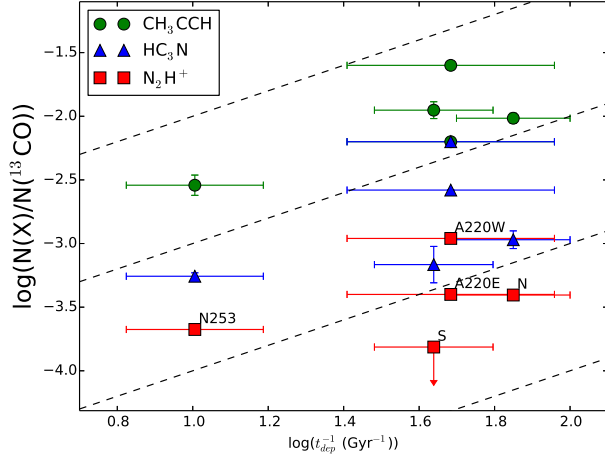


**Figure 15.** Column density ratios of  $\text{CH}_3\text{CCH}$ ,  $\text{HC}_3\text{N}$ , and  $\text{N}_2\text{H}^+$  over  $^{13}\text{CO}$  are shown as a function of an inverse of the depletion times, which is proportional to the star formation efficiencies. Note that separate values of star formation efficiencies in the two nuclei of Arp 220 could not be obtained, and the same value is used for the Eastern and Western nuclei. The case of  $N(X)/N(^{13}\text{CO}) \propto \tau_{\text{dep}}^{-1}$  are shown in dotted lines for a reference.

**Table 1.** Observational Parameters.

ID	Array	Cycle	config	Observation date	$N_{ant}$	Baseline Range (m)	$T_{on}$ (min)	LSB range (GHz)	USB range (GHz)
PI data (2015.1.00412.S, 2016.1.00965.S)									
Band3_a	12 m	3	C40-3	2016-5-28	39	15 - 704.1	47.3	85.49-89.07	97.24-100.89
	12 m	4	C40-6	2016-10-29	40	18.4 - 1107.2	46.7		
Band3_b	12m	3	C40-3	2016-5-28	36	15.7 -649.4	46.2	88.91-92.49	100.91-104.49
	12 m	4	C40-6	2016-10-22	39	18.2-1291.2	13.1		
Band3_c	12 m	3	C36-2/3	2016-4-30	40	14.6 -627.6	40.8	94.71-98.29	106.71-110.29
Band6_a	12 m	3	C36-2/3	2016-4-1	43	14.0 -431.0	11.4	214.06-217.71	230.06-233.71
	7m	4	...	2016-10-08	10	7.4-44.2	18.1		
Band6_b	12 m	3	C36-2/3	2016-4-2	42	14.1 -429.7	9.9	217.61-221.26	233.61-237.26
Band6_c	12 m	3	C36-2/3	2016-4-2	42	14.3 -425	9.9	221.16-224.81	237.16-240.81
Band6_d	12 m	3	C36-2/3	2016-4-2	42	14.0 -418.9	9.9	224.71-228.36	240.71-244.36
Band6_e	12 m	3	C36-2/3	2016-4-2	42	13.4 -404.0	10.9	244.79- 248.43	258.98-262.62
	12 m	4	C40-4	2016-11-28	45	16.1-701.2	10.9		
	7m	4	...	2016-10-14	9	9.0-43.6	18.1		
Band6_f	12 m	3	C36-2/3	2016-4-2	42	13.7 -412	10.4	248.32-251.96	262.51-266.15
	7m	4	...	2016-10-11	10	9.0 - 44.5	17.6		
Band6_g	12 m	3	C36-2/3	2016-4-9	42	12.9 -395.5	10.4	251.87-255.51	266.06-269.70
	7m	4	...	2016-10-05	8	7.5-39.6	17.1		
Band6_h	12 m	3	C36-2/3	2016-4-10	40	14.1 -420.1	10.4	255.44-259.08	269.63-273.27
	12 m	4	C40-4	2016-11-29	43	13.5 - 632.0	10.4		
	7m	4	...	2016-10-21	9	7.6-44.1	17.6		
Archive Data (2015.1.00993.S)									
Band3_a	12 m	3	C36-1/2	2016-3-4	42	13.6-429.4	33.3	84.26-87.63	96.30-99.86
	12 m	3	C36-1/2	2016-3-7	40	13.7-429.4	33.3		
Band3_b	12m	3	C36-1/2	2016-3-7	40	12.6 - 428.0	32.8	86.89 - 90.45	98.93-102.49
	12 m	3	C36-2/3	2016-3-8	44	13.1-438.9	32.8		
Band3_c	12 m	3	C36-2/3	2016-3-9	41	13.9 - 428.2	33.8	94.56 - 97.83	106.06 - 109.62
	12 m	3	C36-2/3	2016-3-11	39	13.6 - 426.3	33.8		

**Table 2.** Image parameters used to create the moment 0 maps in Figures 4-5 and their cube properties. For the weighting, *roba* indicates that it was imaged with a robust parameter *a*, and *robtpb* indicates that it was imaged with a robust parameter *a* while using uv-taper of outer baselines less than *b''*.

Line	weighting	beam size (")	rms (mJy/beam km/s)
$^{13}\text{CO}(1-0)$	rob1	$1.50 \times 1.44$	31.7
$^{13}\text{CO}(2-1)$	rob2tp0.5	$1.06 \times 0.98$	82.9
$\text{C}^{18}\text{O}(1-0)$	rob1	$1.51 \times 1.44$	19.8
$\text{C}^{18}\text{O}(2-1)$	rob2tp0.5	$1.07 \times 1.01$	56.1
$\text{HCN}(1-0)$	rob0	$0.73 \times 0.61$	28.5
$\text{HCN}(3-2)$	rob2tp0.5	$0.94 \times 0.91$	81.6
$\text{HCO}^+(1-0)$	rob0	$0.73 \times 0.61$	30.4
$\text{HCO}^+(3-2)$	rob2tp0.5	$0.94 \times 0.90$	113.6
$\text{HNC}(1-0)$	rob2	$1.69 \times 1.48$	21.0
$\text{HNC}(3-2)$	rob2tp0.5	$0.98 \times 0.87$	71.6
$\text{CS}(2-1)$	rob1	$1.65 \times 1.60$	20.7
$\text{CS}(5-4)$	rob2tp0.5	$1.00 \times 0.94$	64.6
$\text{CH}_3\text{OH}(2_k-1_k)$	rob1	$1.68 \times 1.62$	17.9
$\text{CH}_3\text{OH}(5_k-4_k)$	rob2tp0.5	$0.99 \times 0.94$	67.8
$\text{CCH}(1-0)$	rob2	$1.37 \times 1.16$	31.2
$\text{CCH}(3-2)$	rob2tp0.5	$0.81 \times 0.73$	64.1
$\text{CN}(2-1)$	rob2tp0.5	$1.03 \times 1.01$	129.1
$\text{SiO}(2-1)$	rob2	$1.56 \times 1.32$	16.4
$\text{H40}\alpha$	rob2	$1.38 \times 1.22$	12.4
$\text{N}_2\text{H}^+(1-0)$	rob2	$1.15 \times 1.06$	35.4
$\text{CH}_3\text{CCH}(6_k-5_k)$	rob2	$1.50 \times 1.32$	19.7
$\text{CH}_3\text{CCH}(13_k-12_k)$	rob2tp0.5	$1.07 \times 1.01$	63.6
$\text{HC}_3\text{N}(12-11)$	rob1	$1.50 \times 1.45$	18.6
$\text{HC}_3\text{N}(10-9)$	rob2	$1.68 \times 1.47$	19.6

**Table 3.** Values of rms in each scheduling block after the beam was convolved to  $1.7'' \times 1.7''$

ID	$f_{range}$ (GHz)	band	rms (mJy/beam)
Band3_a1	85.49 - 87.63	LSB	0.181
Band3_a1	97.24 - 99.86	USB	0.215
Band3_a2	87.63 - 89.07	LSB	0.193
Band3_a2	99.86- 100.89	USB	0.217
Band3_b1	88.91- 90.45	LSB	0.181
Band3_b1	100.91 - 102.49	USB	0.200
Band3_b2	90.45 - 92.49	LSB	0.484
Band3_b2	102.49 - 104.49	USB	0.533
Band3_c	94.71 - 97.83	LSB	0.165
Band3_c	106.71- 109.62	USB	0.192
Band6_a	214.06-217.71	LSB	0.633
Band6_a	230.06-233.71	USB	0.692
Band6_b	217.61-221.26	LSB	0.898
Band6_b	233.61-237.26	USB	0.932
Band6_c	221.16-224.81	LSB	0.793
Band6_c	237.16-240.81	USB	0.860
Band6_d	224.71-228.36	LSB	0.867
Band6_d	240.71-244.36	USB	0.993
Band6_e	244.79- 248.43	LSB	0.847
Band6_e	258.98-262.62	USB	0.931
Band6_f	248.32-251.96	LSB	1.002
Band6_f	262.51-266.15	USB	1.202
Band6_g	251.87-255.51	LSB	0.869
Band6_g	266.06-269.70	USB	1.043
Band6_h	255.44-259.08	LSB	0.888
Band6_h	269.63-273.27	USB	1.047



**Table 4.** Properties of the central molecular zones of NGC 253, NGC 3256, and Arp 220. Distances from the earth  $D$ , star formation rates SFR, molecular masses  $M_{\text{mol}}$ , and depletion times  $\tau_{\text{dep}}$  ( $\equiv M_{\text{mol}}/\text{SFR}$ ;  $\tau_{\text{dep}}^{-1}$  is an indication of star formation efficiency). References are a) Tully et al. (2013) b) Sanders et al. (2003), c) Barcos-Muñoz et al. (2015) d) Leroy et al. (2015) e) Lira et al. (2008) f) Sorai et al. (2000) g) Sakamoto et al. (2014)

Galaxy	$D$ (Mpc)	SFR( $M_{\odot} \text{ yr}^{-1}$ )	$M_{\text{mol}}(M_{\odot})$	$\tau_{\text{dep}}$ (yr)
NGC 253	$3.5^a$	$2^d$	$(1.3 - 3) \times 10^{8d,f}$	$(0.65 - 1.5) \times 10^8$
NGC 3256	$35^b$	$15(\text{N})^e$	$(1.5 - 3) \times 10^{8,g}$	$(1 - 2) \times 10^7$
		$6(\text{S})^e$	$(1 - 2) \times 10^{8,g}$	$(1.6 - 3.3) \times 10^7$
Arp220	$80^b$	$180^c$	$(2 - 7) \times 10^{9c}$	$(1.1 - 3.9) \times 10^7$

**Table 5.** Column densities at N

Molecule	N ( $\text{cm}^{-2}$ )	T <sub>ex</sub> (K)
$^{13}\text{CO}$	$(3.0 \pm 0.1) \times 10^{16.0}$	$10.5 \pm 0.6$
	$(2.3 \pm 0.1) \times 10^{16.0}$	$11.5 \pm 0.7$
$\text{C}^{18}\text{O}$	$(1.2 \pm 0.1) \times 10^{16.0}$	$11.8 \pm 1.4$
	$(9.1 \pm 0.6) \times 10^{15.0}$	$11.5 \pm 1.3$
$\text{C}^{17}\text{O}$	$(9.8 \pm 1.8) \times 10^{14.0}$	$10.5 \pm \dots$
	$(1.1 \pm 0.1) \times 10^{15.0}$	$11.3 \pm \dots$
$\text{HCN}$	$(2.4 \pm 0.1) \times 10^{14.0}$	$6.0 \pm 0.0$
	$(1.5 \pm 0.1) \times 10^{14.0}$	$6.1 \pm 0.0$
$\text{HCO}^+$	$(1.3 \pm 0.1) \times 10^{14.0}$	$6.5 \pm 0.1$
	$(1.0 \pm 0.1) \times 10^{14.0}$	$6.9 \pm 0.1$
$\text{HNC}$	$(1.1 \pm 0.1) \times 10^{14.0}$	$6.3 \pm 0.1$
	$(8.3 \pm 0.5) \times 10^{13.0}$	$6.0 \pm 0.1$
$\text{CS}$	$(1.1 \pm 0.1) \times 10^{14.0}$	$9.6 \pm 0.2$
	$(1.0 \pm 0.1) \times 10^{14.0}$	$8.8 \pm 0.2$
$\text{CN}$	$(1.4 \pm 0.1) \times 10^{15.0}$	$5.0 \pm 0.1$
	$(6.4 \pm 0.6) \times 10^{14.0}$	$5.2 \pm 0.1$
$\text{CCH}$	$(1.6 \pm 0.1) \times 10^{15.0}$	$6.8 \pm 0.1$
	$(1.1 \pm 0.1) \times 10^{15.0}$	$6.7 \pm 0.1$
$\text{CH}_3\text{OH}$	$(7.6 \pm 0.5) \times 10^{13.0}$	$15.0 \pm \dots$
	$(5.1 \pm 0.5) \times 10^{13.0}$	$15.0 \pm \dots$
$\text{H}_2\text{CO}$	$(1.2 \pm 0.1) \times 10^{13.0}$	$18.5 \pm 4.3$
	$(1.4 \pm 0.3) \times 10^{13.0}$	$35.1 \pm 13.2$
$\text{NNH}^+$	$(1.3 \pm 0.1) \times 10^{13.0}$	$10.0 \pm \dots$
	$(8.4 \pm 0.5) \times 10^{12.0}$	$10.0 \pm \dots$
$\text{HCCCN}$	$(3.2 \pm 0.5) \times 10^{13.0}$	$13.4 \pm 1.5$
	$(2.5 \pm 0.3) \times 10^{13.0}$	$22.3 \pm 3.8$
$\text{CH}_3\text{CCH}$	$(2.8 \pm 0.1) \times 10^{14.0}$	$43.0 \pm 1.7$
	$(2.3 \pm 0.1) \times 10^{14.0}$	$45.0 \pm 2.4$
$\text{CH}_3\text{CN}$	$(1.0 \pm 0.0) \times 10^{13.0}$	$10.0 \pm \dots$
	$(6.6 \pm 0.3) \times 10^{12.0}$	$10.0 \pm \dots$
$\text{SiO}$	$(7.6 \pm 0.9) \times 10^{12.0}$	$10.0 \pm \dots$
	$(4.7 \pm 0.8) \times 10^{12.0}$	$10.0 \pm \dots$
$\text{H}^{13}\text{CO}^+$	$(4.6 \pm 1.8) \times 10^{12.0}$	$6.0 \pm 0.7$
	$(4.3 \pm 1.8) \times 10^{12.0}$	$5.1 \pm 0.5$
$\text{HOC}^+$	$(1.8 \pm 1.1) \times 10^{12.0}$	$8.3 \pm 2.1$
	$(1.6 \pm 1.0) \times 10^{12.0}$	$8.5 \pm 2.4$
$\text{c-C}_3\text{H}_2$	$(8.5 \pm 1.6) \times 10^{12.0}$	$17.1 \pm 3.1$
	$(1.2 \pm 0.2) \times 10^{13.0}$	$15.3 \pm 1.6$
$\text{SO}$	$(2.7 \pm 1.7) \times 10^{13.0}$	$10.5 \pm 3.7$
	$(2.5 \pm 1.4) \times 10^{13.0}$	$10.4 \pm 3.3$
$\text{C}^{34}\text{S}$	$(1.7 \pm 0.7) \times 10^{13.0}$	$9.4 \pm 1.4$
	$(1.0 \pm 0.5) \times 10^{13.0}$	$9.8 \pm 2.1$
$\text{NO}$	$(1.0 \pm 0.1) \times 10^{15.0}$	$10.0 \pm \dots$
	$(8.8 \pm 0.6) \times 10^{14.0}$	$10.0 \pm \dots$
$\text{CO}^+$	$(1.1 \pm 0.3) \times 10^{13.0}$	$10.0 \pm \dots$
	$(1.3 \pm 0.2) \times 10^{13.0}$	$10.0 \pm \dots$
$\text{HNCO}$	$(2.5 \pm 0.1) \times 10^{13.0}$	$30.0 \pm \dots$
	$(2.6 \pm 0.1) \times 10^{13.0}$	$30.0 \pm \dots$

**Table 6.** Column densities at S

Molecule	N ( $\text{cm}^{-2}$ )	T <sub>ex</sub> (K)
$^{13}\text{CO}$	$(2.5 \pm 0.2) \times 10^{16.0}$	$10.8 \pm 1.1$
	$(3.4 \pm 0.3) \times 10^{16.0}$	$8.5 \pm 0.6$
$\text{C}^{18}\text{O}$	$(3.8 \pm 0.7) \times 10^{15.0}$	$10.6 \pm 2.8$
	$(6.1 \pm 1.3) \times 10^{15.0}$	$6.7 \pm 0.9$
$\text{C}^{17}\text{O}$	$(8.1 \pm 1.2) \times 10^{14.0}$	$10.8 \pm \dots$
	$(1.0 \pm 0.2) \times 10^{15.0}$	$8.5 \pm \dots$
$\text{HCN}$	$(8.8 \pm 0.4) \times 10^{13.0}$	$5.6 \pm 0.1$
	$(4.9 \pm 0.4) \times 10^{13.0}$	$5.8 \pm 0.1$
$\text{HCO}^+$	$(8.5 \pm 0.3) \times 10^{13.0}$	$6.7 \pm 0.1$
	$(4.3 \pm 0.3) \times 10^{13.0}$	$7.3 \pm 0.2$
$\text{HNC}$	$(4.3 \pm 0.4) \times 10^{13.0}$	$6.1 \pm 0.2$
	$(1.3 \pm 0.3) \times 10^{13.0}$	$6.2 \pm 0.4$
$\text{CS}$	$(7.8 \pm 0.9) \times 10^{13.0}$	$8.2 \pm 0.2$
	$(5.3 \pm 0.8) \times 10^{13.0}$	$8.6 \pm 0.3$
$\text{CN}$	$(3.8 \pm 0.1) \times 10^{14.0}$	$5.1 \pm 0.1$
	$(1.3 \pm 0.1) \times 10^{14.0}$	$5.3 \pm 0.1$
$\text{CCH}$	$(9.5 \pm 0.4) \times 10^{14.0}$	$6.9 \pm 0.1$
	$(5.1 \pm 0.4) \times 10^{14.0}$	$7.0 \pm 0.2$
$\text{CH}_3\text{OH}$	$(4.8 \pm 0.3) \times 10^{13.0}$	$18.8 \pm 1.4$
	$(1.5 \pm 0.1) \times 10^{14.0}$	$9.2 \pm 0.4$
$\text{H}_2\text{CO}$	$(1.5 \pm 0.9) \times 10^{13.0}$	$40.7 \pm 25.6$
	$(6.0 \pm 1.4) \times 10^{12.0}$	$20.1 \pm 8.9$
$\text{NNH}^+$	$< 4.0 \times 10^{12.0}$	...
	$< 5.0 \times 10^{12.0}$	...
$\text{HCCCN}$	$(1.7 \pm 0.5) \times 10^{13.0}$	$13.0 \pm 2.6$
	$(2.2 \pm 0.7) \times 10^{13.0}$	$10.2 \pm 1.6$
$\text{CH}_3\text{CCH}$	$(2.7 \pm 0.2) \times 10^{14.0}$	$36.3 \pm 1.5$
	$(3.8 \pm 0.3) \times 10^{14.0}$	$31.8 \pm 1.4$
$\text{CH}_3\text{CN}$	$< 3.6 \times 10^{12.0}$	...
	$< 4.8 \times 10^{12.0}$	...
$\text{SiO}$	$(1.9 \pm 0.7) \times 10^{12.0}$	$10.0 \pm \dots$
	$(4.6 \pm 0.8) \times 10^{12.0}$	$10.0 \pm \dots$
$\text{H}^{13}\text{CO}^+$	$< 2.1 \times 10^{12.0}$	...
	$< 2.1 \times 10^{12.0}$	...
$\text{HOC}^+$	$(1.6 \pm 0.3) \times 10^{12.0}$	$10.0 \pm \dots$
	$(1.8 \pm 0.3) \times 10^{12.0}$	$10.0 \pm \dots$
$\text{c-C}_3\text{H}_2$	$< 8.3 \times 10^{12.0}$	...
	$< 1.1 \times 10^{13.0}$	...
$\text{SO}$	$(3.3 \pm 0.6) \times 10^{13.0}$	$10.0 \pm \dots$
	$(4.1 \pm 0.5) \times 10^{13.0}$	$10.0 \pm \dots$
$\text{C}^{34}\text{S}$	$(2.8 \pm 1.3) \times 10^{12.0}$	$8.2 \pm \dots$
	$(3.7 \pm 1.5) \times 10^{12.0}$	$8.6 \pm \dots$
$\text{NO}$	$(5.5 \pm 0.6) \times 10^{14.0}$	$10.0 \pm \dots$
	$(8.6 \pm 0.8) \times 10^{14.0}$	$10.0 \pm \dots$
$\text{CO}^+$	$< 1.1 \times 10^{13.0}$	...
	$< 1.4 \times 10^{13.0}$	...
$\text{HNCO}$	$< 1.1 \times 10^{13.0}$	...
	$< 1.4 \times 10^{13.0}$	...

**Table 7.** Column densities at C

Molecule	N ( $\text{cm}^{-2}$ )	T <sub>ex</sub> (K)
$^{13}\text{CO}$	$(3.7 \pm 0.3) \times 10^{16.0}$	$8.1 \pm 0.6$
$\text{C}^{18}\text{O}$	$(1.1 \pm 0.1) \times 10^{16.0}$	$8.4 \pm 0.7$
$\text{C}^{17}\text{O}$	$(10.0 \pm 3.5) \times 10^{14.0}$	$8.1 \pm \dots$
HCN	$(1.8 \pm 0.1) \times 10^{14.0}$	$5.3 \pm 0.1$
$\text{HCO}^+$	$(1.4 \pm 0.1) \times 10^{14.0}$	$6.1 \pm 0.1$
HNC	$(6.6 \pm 0.7) \times 10^{13.0}$	$4.9 \pm 0.1$
CS	$(1.3 \pm 0.1) \times 10^{14.0}$	$7.5 \pm 0.2$
CN	$(7.8 \pm 0.3) \times 10^{14.0}$	$4.2 \pm 0.0$
CCH	$(1.4 \pm 0.1) \times 10^{15.0}$	$5.3 \pm 0.1$
$\text{CH}_3\text{OH}$	$(4.3 \pm 0.2) \times 10^{14.0}$	$9.6 \pm 0.3$
$\text{H}_2\text{CO}$	$(9.3 \pm 1.5) \times 10^{12.0}$	$18.3 \pm 6.3$
$\text{NNH}^+$	$(6.5 \pm 0.2) \times 10^{12.0}$	$10.0 \pm \dots$
HCCCN	$(4.4 \pm 1.4) \times 10^{13.0}$	$11.5 \pm 2.1$
$\text{CH}_3\text{CCH}$	$(2.1 \pm 0.3) \times 10^{14.0}$	$28.8 \pm 1.8$
$\text{CH}_3\text{CN}$	$(7.5 \pm 0.5) \times 10^{12.0}$	$10.0 \pm \dots$
SiO	$(8.5 \pm 1.2) \times 10^{12.0}$	$10.0 \pm \dots$
$\text{H}^{13}\text{CO}^+$	$(2.6 \pm 0.6) \times 10^{12.0}$	$6.1 \pm \dots$
$\text{HOC}^+$	$(5.6 \pm 0.4) \times 10^{12.0}$	$10.0 \pm \dots$
c- $\text{C}_3\text{H}_2$	$< 7.9 \times 10^{12.0}$	$\dots$
SO	$(6.6 \pm 0.7) \times 10^{13.0}$	$10.0 \pm \dots$
$\text{C}^{34}\text{S}$	$(9.5 \pm 2.1) \times 10^{12.0}$	$7.5 \pm \dots$
NO	$(1.1 \pm 0.1) \times 10^{15.0}$	$10.0 \pm \dots$
$\text{CO}^+$	$< 1.3 \times 10^{13.0}$	$\dots$
HNCO	$(6.2 \pm 0.5) \times 10^{13.0}$	$17.9 \pm 5.7$

**Table 8.** Column densities at TNE

Molecule	N (cm <sup>-2</sup> )	T <sub>ex</sub> (K)
<sup>13</sup> CO	$(3.5 \pm 0.4) \times 10^{16.0}$	$8.3 \pm 0.8$
C <sup>18</sup> O	$(5.4 \pm 1.0) \times 10^{15.0}$	$8.8 \pm 1.6$
C <sup>17</sup> O	$< 7.9 \times 10^{14.0}$	...
HCN	$(7.7 \pm 0.4) \times 10^{13.0}$	$5.0 \pm 0.1$
HCO <sup>+</sup>	$(7.5 \pm 1.2) \times 10^{13.0}$	$6.3 \pm 0.3$
HNC	$(3.2 \pm 0.7) \times 10^{13.0}$	$5.2 \pm 0.3$
CS	$(5.6 \pm 1.1) \times 10^{13.0}$	$6.8 \pm 0.4$
CN	$(2.1 \pm 0.2) \times 10^{14.0}$	$4.5 \pm 0.1$
CCH	$(5.8 \pm 0.8) \times 10^{14.0}$	$5.8 \pm 0.2$
CH <sub>3</sub> OH	$(1.4 \pm 0.1) \times 10^{14.0}$	$9.8 \pm 0.6$
H <sub>2</sub> CO	$(8.9 \pm 1.5) \times 10^{12.0}$	$18.3 \pm 6.8$
NNH <sup>+</sup>	$< 4.6 \times 10^{12.0}$	...
HCCCN	$(1.7 \pm 1.1) \times 10^{13.0}$	$10.7 \pm 3.9$
CH <sub>3</sub> CCH	$(2.8 \pm 0.4) \times 10^{14.0}$	$29.3 \pm 1.9$
CH <sub>3</sub> CN	$< 4.6 \times 10^{12.0}$	...
SiO	$< 3.3 \times 10^{12.0}$	...
H <sup>13</sup> CO <sup>+</sup>	$(2.5 \pm 0.6) \times 10^{12.0}$	$6.3 \pm ...$
HOC <sup>+</sup>	$(1.9 \pm 0.2) \times 10^{12.0}$	$10.0 \pm ...$
c-C <sub>3</sub> H <sub>2</sub>	$(7.1 \pm 3.4) \times 10^{12.0}$	$10.0 \pm ...$
SO	$(4.4 \pm 0.5) \times 10^{13.0}$	$20.0 \pm ...$
C <sup>34</sup> S	$< 6.3 \times 10^{12.0}$	...
NO	$(8.0 \pm 1.1) \times 10^{14.0}$	$10.0 \pm ...$
CO <sup>+</sup>	$< 8.7 \times 10^{12.0}$	...
HNCO	$(2.3 \pm 0.7) \times 10^{13.0}$	$7.3 \pm 2.3$



**Table 9.** Column densities at TSE

Molecule	N (cm <sup>-2</sup> )	T <sub>ex</sub> (K)
<sup>13</sup> CO	$(2.9 \pm 0.4) \times 10^{16.0}$	$6.9 \pm 0.6$
C <sup>18</sup> O	$(5.3 \pm 1.5) \times 10^{15.0}$	$5.4 \pm 0.7$
C <sup>17</sup> O	$< 1.0 \times 10^{15.0}$	...
HCN	$(7.2 \pm 0.4) \times 10^{13.0}$	$5.1 \pm 0.1$
HCO <sup>+</sup>	$(7.3 \pm 1.0) \times 10^{13.0}$	$5.7 \pm 0.2$
HNC	$(2.5 \pm 1.1) \times 10^{13.0}$	$4.8 \pm 0.5$
CS	$(6.9 \pm 1.6) \times 10^{13.0}$	$7.0 \pm 0.6$
CN	$(3.4 \pm 0.6) \times 10^{14.0}$	$3.4 \pm 0.1$
CCH	$(5.2 \pm 1.3) \times 10^{14.0}$	$4.4 \pm 0.2$
CH <sub>3</sub> OH	$(4.5 \pm 0.5) \times 10^{14.0}$	$8.3 \pm 0.5$
H <sub>2</sub> CO	$(1.0 \pm 0.2) \times 10^{13.0}$	$20.0 \pm ...$
NNH <sup>+</sup>	$(7.2 \pm 1.0) \times 10^{12.0}$	$10.0 \pm ...$
HCCCN	$< 1.6 \times 10^{13.0}$	...
CH <sub>3</sub> CCH	$(1.2 \pm 0.4) \times 10^{14.0}$	$24.8 \pm 5.2$
CH <sub>3</sub> CN	$(6.2 \pm 0.8) \times 10^{12.0}$	$10.0 \pm ...$
SiO	$< 5.0 \times 10^{12.0}$	...
H <sup>13</sup> CO <sup>+</sup>	$< 2.5 \times 10^{12.0}$	...
HOC <sup>+</sup>	$< 2.0 \times 10^{12.0}$	...
c-C <sub>3</sub> H <sub>2</sub>	$< 2.0 \times 10^{13.0}$	...
SO	$(3.6 \pm 0.7) \times 10^{13.0}$	$10.0 \pm ...$
C <sup>34</sup> S	$< 7.9 \times 10^{12.0}$	...
NO	$< 1.0 \times 10^{15.0}$	...
CO <sup>+</sup>	$< 1.6 \times 10^{13.0}$	...
HNCO	$< 2.0 \times 10^{13.0}$	...

**Table 10.** Column densities at TSW

Molecule	N ( $\text{cm}^{-2}$ )	T <sub>ex</sub> (K)
$^{13}\text{CO}$	$(3.0 \pm 0.3) \times 10^{16.0}$	$5.6 \pm 0.3$
$\text{C}^{18}\text{O}$	$(6.9 \pm 1.5) \times 10^{15.0}$	$4.9 \pm 0.4$
$\text{C}^{17}\text{O}$	$< 1.3 \times 10^{15.0}$	...
$\text{HCN}$	$(1.2 \pm 0.1) \times 10^{14.0}$	$4.4 \pm 0.1$
$\text{HCO}^+$	$(9.9 \pm 1.8) \times 10^{13.0}$	$4.8 \pm 0.2$
$\text{HNC}$	$(3.1 \pm 0.9) \times 10^{13.0}$	$4.3 \pm 0.3$
$\text{CS}$	$(7.3 \pm 1.5) \times 10^{13.0}$	$6.1 \pm 0.5$
$\text{CN}$	$(4.4 \pm 0.7) \times 10^{14.0}$	$3.4 \pm 0.1$
$\text{CCH}$	$(9.3 \pm 2.5) \times 10^{14.0}$	$3.9 \pm 0.2$
$\text{CH}_3\text{OH}$	$(5.4 \pm 0.4) \times 10^{14.0}$	$7.6 \pm 0.3$
$\text{H}_2\text{CO}$	$(1.0 \pm 0.3) \times 10^{13.0}$	$10.0 \pm \dots$
$\text{NNH}^+$	$(7.8 \pm 0.8) \times 10^{12.0}$	$10.0 \pm \dots$
$\text{HCCCN}$	$(1.8 \pm 0.9) \times 10^{13.0}$	$10.9 \pm 2.9$
$\text{CH}_3\text{CCH}$	$(1.1 \pm 0.2) \times 10^{14.0}$	$24.9 \pm 2.8$
$\text{CH}_3\text{CN}$	$< 4.0 \times 10^{13.0}$	...
$\text{SiO}$	$(8.3 \pm 1.5) \times 10^{12.0}$	$10.0 \pm \dots$
$\text{H}^{13}\text{CO}^+$	$< 1.6 \times 10^{12.0}$	...
$\text{HOC}^+$	$< 1.6 \times 10^{12.0}$	...
$\text{c-C}_3\text{H}_2$	$< 7.9 \times 10^{12.0}$	...
$\text{SO}$	$(4.9 \pm 0.5) \times 10^{13.0}$	$7.7 \pm 3.1$
$\text{C}^{34}\text{S}$	$(9.2 \pm 2.4) \times 10^{12.0}$	$6.1 \pm \dots$
$\text{NO}$	$< 7.9 \times 10^{14.0}$	...
$\text{CO}^+$	$< 1.3 \times 10^{13.0}$	...
$\text{HNCO}$	$(6.3 \pm 0.6) \times 10^{13.0}$	$6.9 \pm 0.6$

**Table 11.** Column densities at OS

Molecule	N (cm <sup>-2</sup> )	T <sub>ex</sub> (K)
<sup>13</sup> CO	$(1.0 \pm 0.4) \times 10^{16.0}$	$5.2 \pm 0.9$
	$< 6.4 \times 10^{15.0}$	...
C <sup>18</sup> O	$(3.1 \pm 2.2) \times 10^{15.0}$	$4.2 \pm 0.9$
	$(8.8 \pm 2.2) \times 10^{14.0}$	$5.0 \pm ...$
C <sup>17</sup> O	$< 1.1 \times 10^{15.0}$	...
	$< 1.9 \times 10^{15.0}$	...
HCN	$(4.2 \pm 0.3) \times 10^{13.0}$	$4.9 \pm 0.1$
	$(2.7 \pm 0.3) \times 10^{13.0}$	$5.6 \pm 0.1$
HCO <sup>+</sup>	$(4.3 \pm 0.5) \times 10^{13.0}$	$5.0 \pm 0.1$
	$(2.4 \pm 0.4) \times 10^{13.0}$	$5.3 \pm 0.2$
HNC	$(1.3 \pm 0.1) \times 10^{13.0}$	$5.0 \pm ...$
	$(7.1 \pm 0.7) \times 10^{12.0}$	$5.0 \pm ...$
CS	$(3.1 \pm 0.8) \times 10^{13.0}$	$7.2 \pm 0.6$
	$(1.5 \pm 0.7) \times 10^{13.0}$	$7.2 \pm ...$
CN	$(1.1 \pm 0.1) \times 10^{14.0}$	$3.9 \pm 0.1$
	$(1.2 \pm 0.1) \times 10^{14.0}$	$3.9 \pm 0.1$
CCH	$(2.7 \pm 0.2) \times 10^{14.0}$	$5.0 \pm ...$
	$(2.1 \pm 1.8) \times 10^{13.0}$	$5.0 \pm ...$
CH <sub>3</sub> OH	$(1.6 \pm 0.1) \times 10^{14.0}$	$11.5 \pm 0.6$
	$(6.4 \pm 1.1) \times 10^{13.0}$	$9.6 \pm 1.2$
H <sub>2</sub> CO	$< 5.8 \times 10^{12.0}$	...
	$< 5.8 \times 10^{12.0}$	...
NNH <sup>+</sup>	$< 4.4 \times 10^{12.0}$	...
	$< 4.4 \times 10^{12.0}$	...
HCCCN	$< 1.3 \times 10^{13.0}$	...
	$< 1.3 \times 10^{13.0}$	...
CH <sub>3</sub> CCH	$< 1.2 \times 10^{14.0}$	...
	$< 1.2 \times 10^{14.0}$	...
CH <sub>3</sub> CN	$< 3.3 \times 10^{12.0}$	...
	$< 3.3 \times 10^{12.0}$	...
SiO	$(4.9 \pm 0.7) \times 10^{12.0}$	$10.0 \pm ...$
	$(2.5 \pm 0.7) \times 10^{12.0}$	$10.0 \pm ...$
H <sup>13</sup> CO <sup>+</sup>	$< 1.9 \times 10^{12.0}$	...
	$< 1.9 \times 10^{12.0}$	...
HOC <sup>+</sup>	$(1.7 \pm 0.3) \times 10^{12.0}$	$7.0 \pm ...$
	$(7.7 \pm 3.5) \times 10^{11.0}$	$7.0 \pm ...$
c-C <sub>3</sub> H <sub>2</sub>	$< 4.4 \times 10^{12.0}$	...
	$< 4.4 \times 10^{12.0}$	...
SO	$(1.9 \pm 0.3) \times 10^{13.0}$	$10.0 \pm ...$
	$(5.3 \pm 3.3) \times 10^{12.0}$	$10.0 \pm ...$
C <sup>34</sup> S	$< 5.8 \times 10^{12.0}$	...
	$< 5.8 \times 10^{12.0}$	...
NO	$< 8.3 \times 10^{14.0}$	...
	$< 8.3 \times 10^{14.0}$	...
CO <sup>+</sup>	$< 1.3 \times 10^{13.0}$	...
	$< 1.3 \times 10^{13.0}$	...
HNCO	$< 1.7 \times 10^{13.0}$	...
	$< 1.7 \times 10^{13.0}$	...

**Table 12.** Column densities at SW

Molecule	N (cm <sup>-2</sup> )	T <sub>ex</sub> (K)
<sup>13</sup> CO	$(6.7 \pm 0.4) \times 10^{16.0}$	$7.8 \pm 0.3$
C <sup>18</sup> O	$(9.8 \pm 0.7) \times 10^{15.0}$	$7.6 \pm 0.4$
C <sup>17</sup> O	$(2.1 \pm 0.3) \times 10^{15.0}$	$7.8 \pm \dots$
HCN	$(1.6 \pm 0.1) \times 10^{14.0}$	$4.9 \pm 0.1$
HCO <sup>+</sup>	$(1.4 \pm 0.1) \times 10^{14.0}$	$6.0 \pm 0.2$
HNC	$(6.2 \pm 0.6) \times 10^{13.0}$	$5.0 \pm 0.1$
CS	$(1.3 \pm 0.1) \times 10^{14.0}$	$7.3 \pm 0.2$
CN	$(6.0 \pm 0.3) \times 10^{14.0}$	$4.1 \pm 0.1$
CCH	$(1.3 \pm 0.1) \times 10^{15.0}$	$5.4 \pm 0.1$
CH <sub>3</sub> OH	$(4.3 \pm 0.1) \times 10^{14.0}$	$10.1 \pm 0.2$
H <sub>2</sub> CO	$(2.3 \pm 0.5) \times 10^{13.0}$	$34.6 \pm 8.9$
NNH <sup>+</sup>	$(1.0 \pm 0.1) \times 10^{13.0}$	$10.0 \pm \dots$
HCCCN	$(3.7 \pm 1.0) \times 10^{13.0}$	$11.1 \pm 1.7$
CH <sub>3</sub> CCH	$(4.1 \pm 0.3) \times 10^{14.0}$	$25.1 \pm 0.9$
CH <sub>3</sub> CN	$< 5.0 \times 10^{12.0}$	$\dots$
SiO	$(8.7 \pm 1.2) \times 10^{12.0}$	$10.0 \pm \dots$
H <sup>13</sup> CO <sup>+</sup>	$(4.6 \pm 0.5) \times 10^{12.0}$	$6.0 \pm \dots$
HOC <sup>+</sup>	$(4.9 \pm 0.5) \times 10^{12.0}$	$10.0 \pm \dots$
c-C <sub>3</sub> H <sub>2</sub>	$(9.2 \pm 2.5) \times 10^{12.0}$	$13.5 \pm 6.3$
SO	$(8.5 \pm 0.8) \times 10^{13.0}$	$10.0 \pm \dots$
C <sup>34</sup> S	$(9.6 \pm 2.6) \times 10^{12.0}$	$7.3 \pm \dots$
NO	$(9.4 \pm 0.7) \times 10^{14.0}$	$10.0 \pm \dots$
CO <sup>+</sup>	$< 1.3 \times 10^{13.0}$	$\dots$
HNCO	$(4.6 \pm 0.4) \times 10^{13.0}$	$9.4 \pm 1.5$

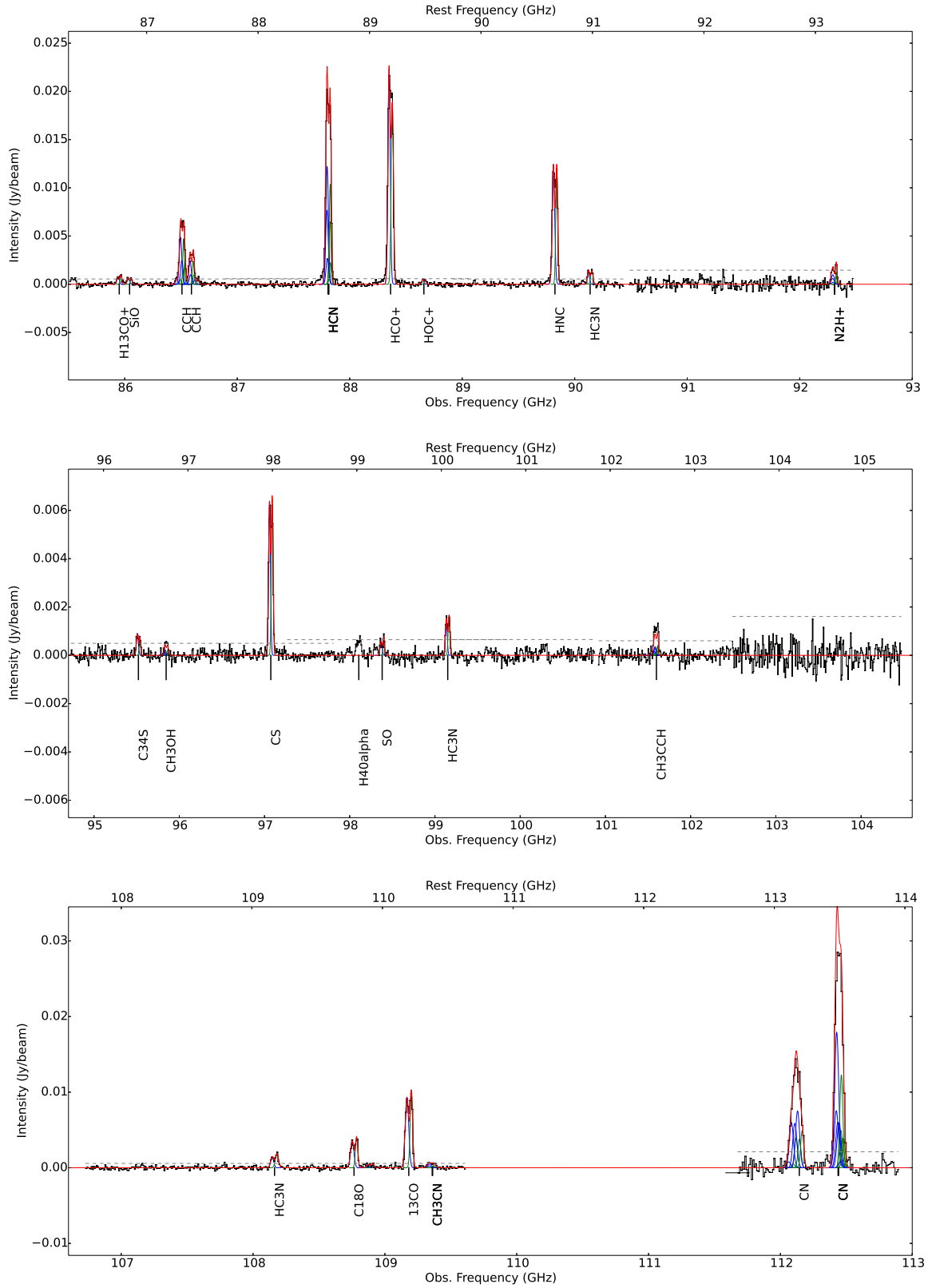


**Figure 16.** Observed spectra from 1.7''-resolution cubes at position N in Band 3. Fitted spectra for individual transitions are shown in blue for component 1 and in green for component 2, while the summed intensities of individual transitions are shown in red. Grey dotted lines show the levels of  $3\sigma$ . The complete figure set (32 images) is available in the online journal of the published version.

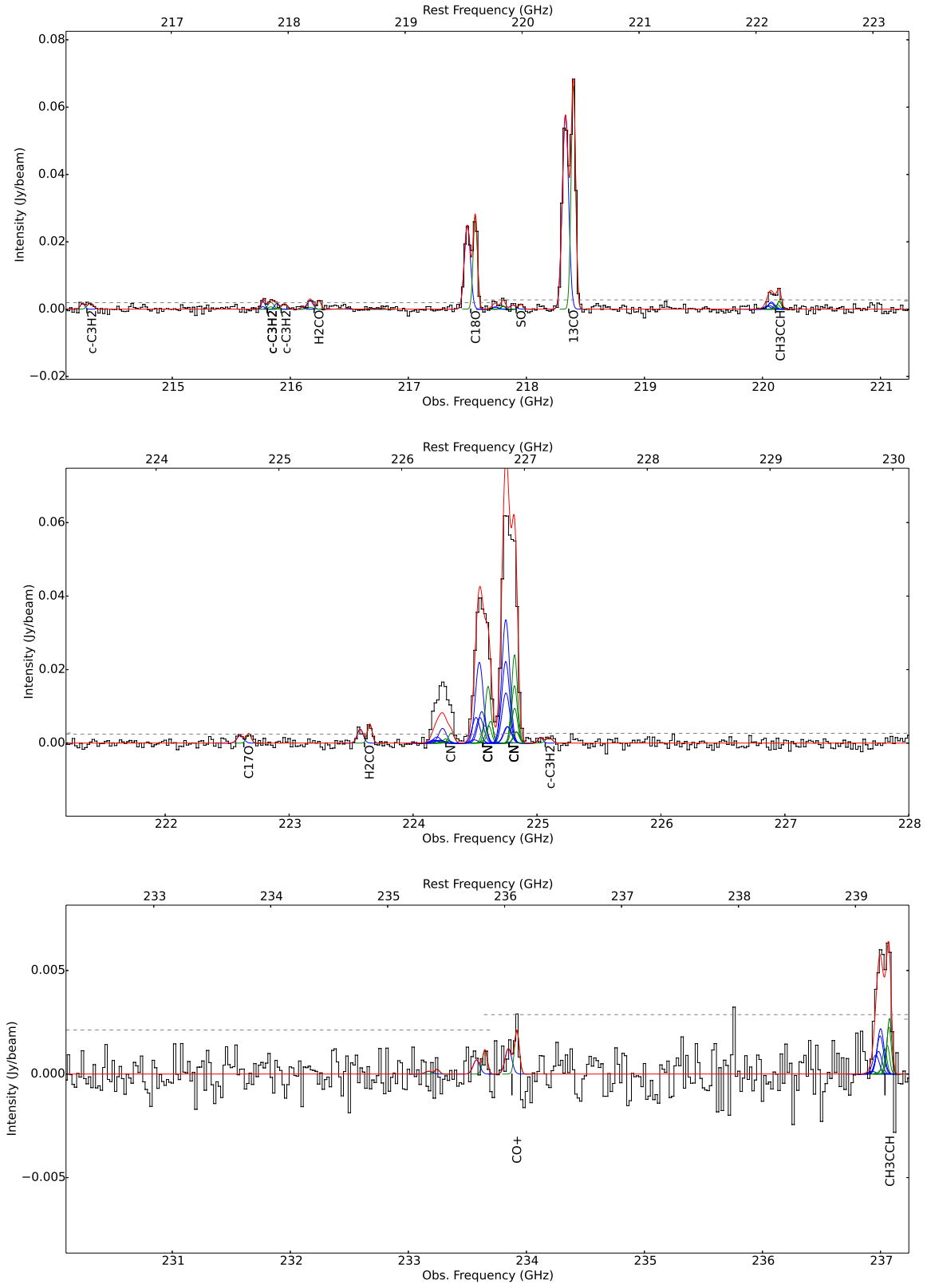


**Figure 17.** Same as Fig 16, but for the Band 6 with sky frequencies 214.1-237.24 (GHz).



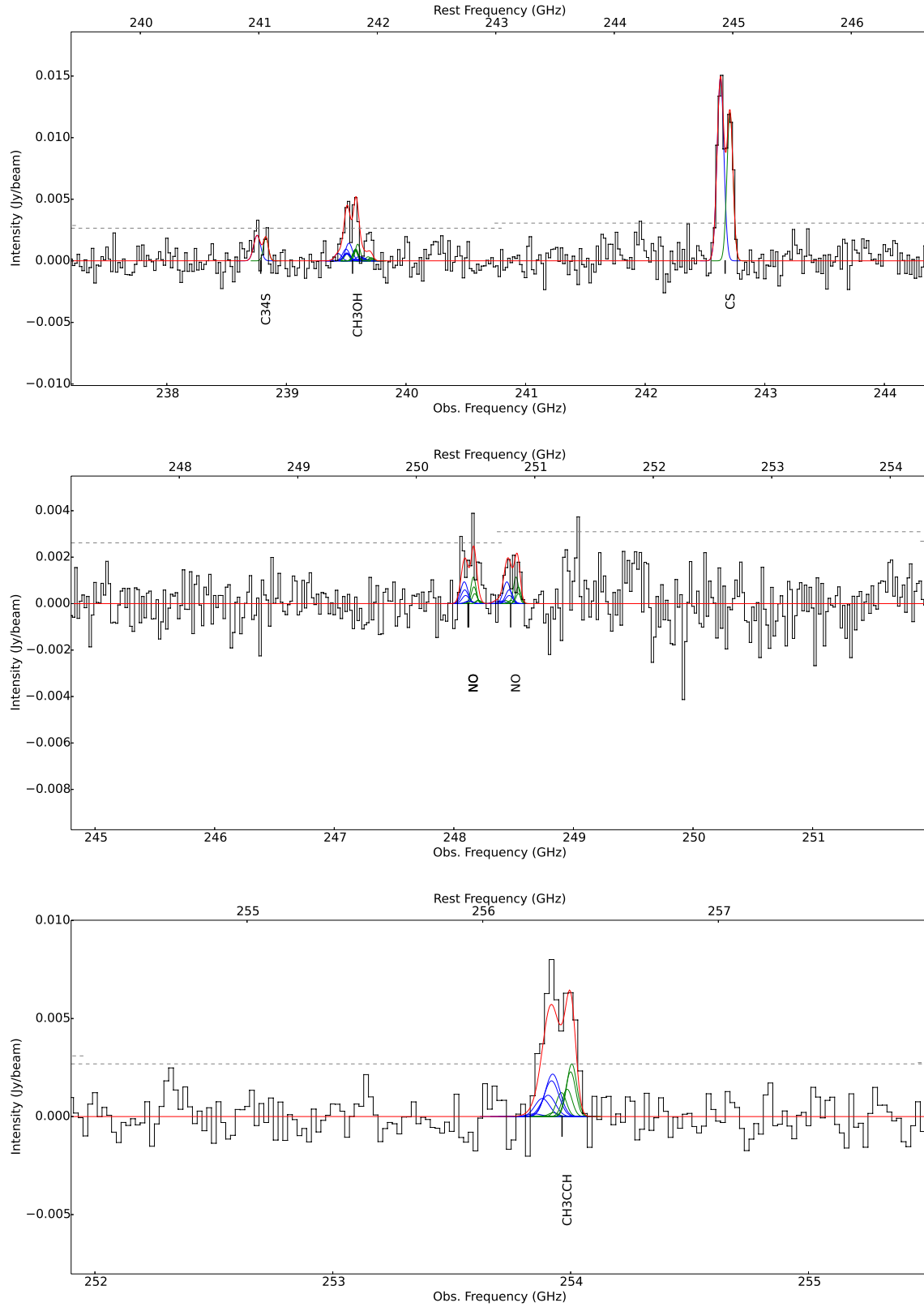


**Figure 18.** Same as Fig 16, but for the Band 6 with sky frequencies 237.2-255.5 (GHz).

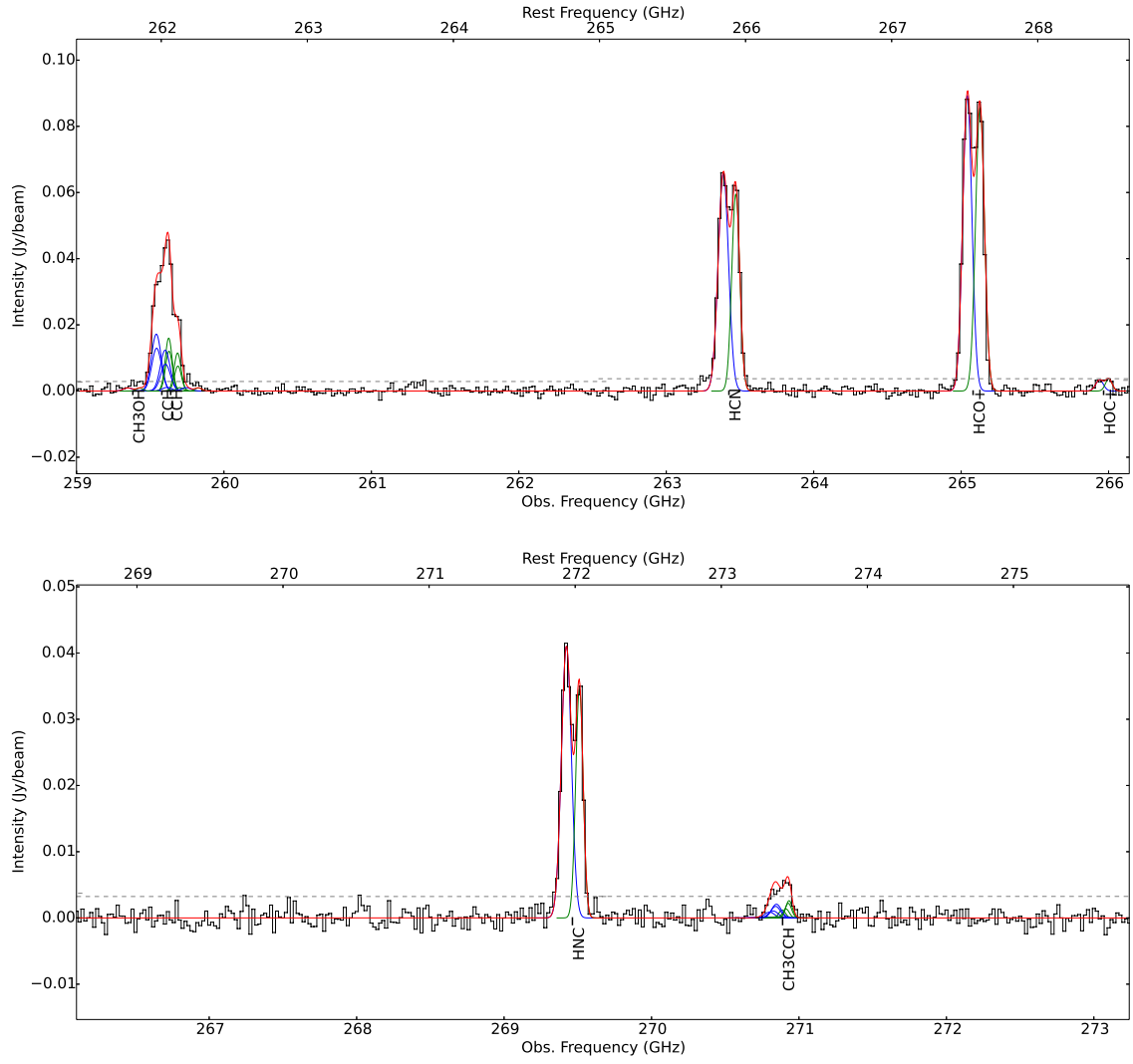


**Figure 19.** Same as Fig 16, but for the Band 6 with sky frequencies 259.0-273.24 (GHz).

**Table 13.** Observed peak intensities and velocity-integrated intensities for detected lines.

Position	Species	Transitions	Restfreq (GHz)	I <sub>peak</sub> (mK)	ΔI <sub>peak</sub> (mK)	I ΔV (K km/s)	Δ(I ΔV) (K km/s)
N	H <sup>13</sup> CO <sup>+</sup>	1 – 0	86.754	56.3	10.41	9.4	0.95
N	SiO	2 – 1	86.847	40.85	10.39	6.41	0.95
N	CCH	1 <sub>3/2</sub> – 0 <sub>1/2</sub>	87.317	373.18	10.28	76.97	0.94
N	CCH	1 <sub>1/2</sub> – 0 <sub>1/2</sub>	87.402	201.53	10.26	41.4	0.94
N	HCN	1 – 0	88.634	1111.22	10.64	197.23	0.96
N	HCO <sup>+</sup>	1 – 0	89.189	1173.21	10.51	205.25	0.95
N	HOC <sup>+</sup>	1 – 0	89.487	26.83	10.44	3.88	0.94
N	HNC	1 – 0	90.664	629.27	9.54	110.23	0.85
N	HC <sub>3</sub> N	10 – 9	90.979	80.17	9.47	11.47	0.85
N	N <sub>2</sub> H <sup>+</sup>	1 – 0	93.176	100.99	24.15	14.96	2.13
N	C <sup>34</sup> S	1 – 0	96.413	38.25	7.69	6.59	0.67
N	CH <sub>3</sub> OH	2 <sub>k</sub> – 1 <sub>k</sub>	96.741	26.23	7.64	3.09	0.66
N	CS	2 – 1	97.981	279.51	7.45	48.99	0.64
N	H40α	—	99.023	35.47	9.50	5.68	0.81
N	SO	2 <sub>1</sub> – 3 <sub>2</sub>	99.3	38.95	9.45	4.99	0.81
N	HC <sub>3</sub> N	11 – 10	100.076	70.48	9.31	10.51	0.79
N	CH <sub>3</sub> CCH	6 <sub>k</sub> – 5 <sub>k</sub>	102.548	54.49	8.25	9.4	0.69
N	HC <sub>3</sub> N	12 – 11	109.174	74.57	6.99	9.63	0.57
N	C <sup>18</sup> O	1 – 0	109.782	135.08	6.91	21.37	0.56
N	HNCO	5 <sub>0,5</sub> – 4 <sub>0,4</sub>	109.906	22.57	6.9	3.5	0.56
N	<sup>13</sup> CO	1 – 0	110.201	349.93	6.86	51.13	0.56
N	CH <sub>3</sub> CN	6 <sub>k</sub> – 5 <sub>k</sub>	110.383	23.73	6.84	4.75	0.55
N	CN	1 <sub>3/2</sub> – 0 <sub>1/2</sub>	113.191	485.15	23.72	101.7	2.12
N	CN	1 <sub>1/2</sub> – 0 <sub>1/2</sub>	113.491	954.47	23.59	178.52	2.11
N	c-C <sub>3</sub> H <sub>2</sub>	3 <sub>3,0</sub> – 2 <sub>2,1</sub>	216.279	18.89	5.97	2.08	0.55
N	c-C <sub>3</sub> H <sub>2</sub>	6 <sub>k</sub> – 5 <sub>k</sub>	217.822	28.73	5.89	4.8	0.54
N	c-C <sub>3</sub> H <sub>2</sub>	5 <sub>1,4</sub> – 4 <sub>2,3</sub>	217.94	28.7	5.88	4.04	0.54
N	c-C <sub>3</sub> H <sub>2</sub>	5 <sub>2,4</sub> – 4 <sub>1,3</sub>	218.16	22.92	5.87	4.25	0.54
N	H <sub>2</sub> CO	3 <sub>0,3</sub> – 2 <sub>0,2</sub>	218.222	22.91	5.87	4.49	0.53
N	H <sub>2</sub> CO	3 <sub>2,2</sub> – 2 <sub>2,1</sub>	218.476	12.87	5.85	1.83	0.53
N	C <sup>18</sup> O	2 – 1	219.56	232.37	5.8	35.09	0.53
N	HNCO	10 <sub>0,10</sub> – 9 <sub>0,9</sub>	219.798	28.75	8.2	3.69	0.75
N	SO	6 <sub>5</sub> – 5 <sub>4</sub>	219.949	28.71	8.19	2.42	0.74
N	<sup>13</sup> CO	2 – 1	220.399	606.9	8.16	85.29	0.74
N	CH <sub>3</sub> CCH	13 <sub>k</sub> – 12 <sub>k</sub>	222.167	54.25	8.03	7.61	0.73
N	C <sup>17</sup> O	2 – 1	224.714	20.81	6.94	2.71	0.62
N	H <sub>2</sub> CO	3 <sub>1,2</sub> – 2 <sub>1,1</sub>	225.698	42.28	6.88	4.84	0.62
N	CN	2 <sub>3/2</sub> – 1 <sub>3/2</sub>	226.36	139.81	6.84	26.33	0.58

*Table 13 continued*

**Table 13** (*continued*)

Position	Species	Transitions	Restfreq (GHz)	I <sub>peak</sub> (mK)	ΔI <sub>peak</sub> (mK)	I ΔV (K km/s)	Δ(I ΔV) (K km/s)
N	CN	$2_{3/2} - 1_{1/2}$	226.66	331.56	6.82	50.92	0.46
N	CN	$2_{5/2} - 1_{3/2}$	226.875	518.34	6.81	91.61	0.58
N	c-C <sub>3</sub> H <sub>2</sub>	$4_{3,2} - 3_{2,1}$	227.169	16.2	7.43	1.97	0.66
N	CO <sup>+</sup>	$2_{3/2} - 1_{1/2}$	235.79	12.47	5.51	1.26	0.48
N	CO <sup>+</sup>	$2_{5/2} - 1_{3/2}$	236.063	22.48	7.41	1.61	0.65
N	CH <sub>3</sub> CCH	$14_k - 13_k$	239.252	47.7	7.22	8.8	0.63
N	C <sup>34</sup> S	$5 - 4$	241.016	24.5	6.56	2.12	0.57
N	CH <sub>3</sub> OH	$5_k - 4_k$	241.791	37.99	6.52	5.84	0.57
N	CS	$5 - 4$	244.936	108.3	7.35	15.45	0.63
N	NO	$5/2 + -3/2 -$	250.483	26.75	6.0	3.18	0.51
N	NO	$5/2 - -3/2 +$	250.817	14.28	7.08	1.54	0.6
N	CH <sub>3</sub> CCH	$15_k - 14_k$	256.337	52.6	5.89	7.66	0.5
N	H <sup>13</sup> CO <sup>+</sup>	$3 - 2$	260.255	19.05	5.84	2.6	0.49
N	CH <sub>3</sub> OH	$2_{1,1} - 1_{0,1}$	261.806	208.08	6.05	13.46	0.5
N	CCH	$3 - 2$	262.004	286.7	6.04	53.6	0.5
N	HCN	$3 - 2$	265.886	402.69	7.58	71.38	0.63
N	HCO <sup>+</sup>	$3 - 2$	267.558	531.35	7.49	91.56	0.62
N	HOC <sup>+</sup>	$3 - 2$	268.451	22.04	7.44	2.8	0.61
N	HNC	$3 - 2$	271.981	241.95	6.3	37.97	0.51
N	CH <sub>3</sub> CCH	$16_k - 15_k$	273.42	32.6	6.26	5.6	0.51
S	SiO	$2 - 1$	86.847	29.12	10.39	2.75	0.95
S	CCH	$1_{3/2} - 0_{1/2}$	87.317	243.63	10.28	37.41	0.94
S	CCH	$1_{1/2} - 0_{1/2}$	87.402	137.71	10.26	20.28	0.94
S	HCN	$1 - 0$	88.634	510.57	10.64	56.68	0.96
S	HCO <sup>+</sup>	$1 - 0$	89.189	773.12	10.51	87.87	0.95
S	HOC <sup>+</sup>	$1 - 0$	89.487	27.53	10.44	3.02	0.94
S	HNC	$1 - 0$	90.664	275.69	9.54	28.08	0.85
S	HC <sub>3</sub> N	$10 - 9$	90.979	40.77	9.48	5.06	0.85
S	C <sup>34</sup> S	$1 - 0$	96.413	17.5	7.7	1.07	0.67
S	CH <sub>3</sub> OH	$2_k - 1_k$	96.741	48.45	7.64	6.22	0.66
S	CS	$2 - 1$	97.981	150.92	7.45	22.92	0.64
S	H40α	—	99.023	34.76	9.51	5.50	0.81
S	SO	$2_1 - 3_2$	99.3	57.63	9.46	6.08	0.81
S	HC <sub>3</sub> N	$11 - 10$	100.076	34.12	9.31	3.49	0.79
S	CH <sub>3</sub> CCH	$6_k - 5_k$	102.548	78.86	8.25	10.22	0.69
S	HC <sub>3</sub> N	$12 - 11$	109.174	26.9	6.99	2.82	0.57
S	C <sup>18</sup> O	$1 - 0$	109.782	73.14	6.92	9.09	0.56
S	<sup>13</sup> CO	$1 - 0$	110.201	419.11	6.86	53.22	0.56
S	CN	$1_{3/2} - 0_{1/2}$	113.191	133.03	23.73	24.62	2.12
S	CN	$1_{1/2} - 0_{1/2}$	113.491	375.3	23.6	48.44	2.11
S	H <sub>2</sub> CO	$3_{0,3} - 2_{0,2}$	218.222	21.13	5.88	1.64	0.54

*Table 13 continued*

**Table 13** (*continued*)

Position	Species	Transitions	Restfreq (GHz)	I <sub>peak</sub> (mK)	ΔI <sub>peak</sub> (mK)	I ΔV (K km/s)	Δ(I ΔV) (K km/s)
S	C <sup>18</sup> O	2 – 1	219.56	87.1	5.81	10.09	0.53
S	<sup>13</sup> CO	2 – 1	220.399	549.1	8.18	66.45	0.74
S	CH <sub>3</sub> CCH	13 <sub>k</sub> – 12 <sub>k</sub>	222.167	55.88	8.05	7.78	0.73
S	C <sup>17</sup> O	2 – 1	224.714	20.62	6.95	2.38	0.62
S	H <sub>2</sub> CO	3 <sub>1,2</sub> – 2 <sub>1,1</sub>	225.698	33.19	6.89	3.31	0.62
S	CN	2 <sub>3/2</sub> – 1 <sub>3/2</sub>	226.36	29.88	6.85	4.86	0.61
S	CN	2 <sub>3/2</sub> – 1 <sub>1/2</sub>	226.66	106.69	6.84	14.88	0.61
S	CN	2 <sub>5/2</sub> – 1 <sub>3/2</sub>	226.875	198.24	6.82	25.84	0.61
S	CH <sub>3</sub> CCH	14 <sub>k</sub> – 13 <sub>k</sub>	239.252	55.34	7.23	6.75	0.63
S	CH <sub>3</sub> OH	5 <sub>k</sub> – 4 <sub>k</sub>	241.791	26.22	6.54	4.35	0.57
S	CS	5 – 4	244.936	41.85	7.36	4.62	0.63
S	NO	5/2 + – 3/2 –	250.483	17.18	6.01	2.06	0.51
S	NO	5/2 – – 3/2 +	250.817	14.49	7.1	2.01	0.6
S	CH <sub>3</sub> CCH	15 <sub>k</sub> – 14 <sub>k</sub>	256.337	39.52	5.9	5.59	0.5
S	CCH	3 – 2	262.004	165.19	6.06	28.91	0.5
S	HCN	3 – 2	265.886	139.89	7.6	17.72	0.63
S	HCO <sup>+</sup>	3 – 2	267.558	371.92	7.51	43.69	0.62
S	HNC	3 – 2	271.981	92.91	6.32	9.16	0.52
S	CH <sub>3</sub> CCH	16 <sub>k</sub> – 15 <sub>k</sub>	273.42	31.35	6.28	4.38	0.51
C	H <sup>13</sup> CO <sup>+</sup>	1 – 0	86.754	28.84	10.38	3.44	0.95
C	SiO	2 – 1	86.847	57.26	10.35	5.26	0.95
C	CCH	1 <sub>3/2</sub> – 0 <sub>1/2</sub>	87.317	281.38	10.24	38.37	0.93
C	CCH	1 <sub>1/2</sub> – 0 <sub>1/2</sub>	87.402	144.99	10.22	18.36	0.93
C	HNCO	4 <sub>0,4</sub> – 3 <sub>0,3</sub>	87.926	55.98	10.1	3.96	0.92
C	HCN	1 – 0	88.634	797.6	10.6	93.15	0.96
C	HCO <sup>+</sup>	1 – 0	89.189	1112.08	10.47	139.46	0.94
C	HOC <sup>+</sup>	1 – 0	89.487	50.54	10.4	5.6	0.94
C	HNC	1 – 0	90.664	384.4	9.5	38.95	0.85
C	HC <sub>3</sub> N	10 – 9	90.979	73.71	9.44	8.03	0.84
C	N <sub>2</sub> H <sup>+</sup>	1 – 0	93.176	101.29	24.06	6.46	2.12
C	C <sup>34</sup> S	1 – 0	96.413	30.82	7.66	2.04	0.66
C	CH <sub>3</sub> OH	2 <sub>k</sub> – 1 <sub>k</sub>	96.741	202.4	7.61	15.26	0.66
C	CS	2 – 1	97.981	316.68	7.42	29.89	0.64
C	H40α	—	99.023	21.03	9.46	0.88	0.81
C	SO	2 <sub>1</sub> – 3 <sub>2</sub>	99.3	51.59	9.41	5.6	0.8
C	HC <sub>3</sub> N	11 – 10	100.076	72.21	9.26	7.15	0.79
C	CH <sub>3</sub> CCH	6 <sub>k</sub> – 5 <sub>k</sub>	102.548	46.12	8.21	4.92	0.69
C	CH <sub>3</sub> OH	0 <sub>0,0</sub> – 1 <sub>1,1</sub>	108.894	42.87	6.99	2.55	0.57
C	HC <sub>3</sub> N	12 – 11	109.174	47.64	6.95	4.42	0.57
C	C <sup>18</sup> O	1 – 0	109.782	158.38	6.87	12.53	0.56
C	HNCO	5 <sub>0,5</sub> – 4 <sub>0,4</sub>	109.906	67.01	6.86	6.18	0.56

*Table 13 continued*

**Table 13** (*continued*)

Position	Species	Transitions	Restfreq (GHz)	I <sub>peak</sub> (mK)	ΔI <sub>peak</sub> (mK)	I ΔV (K km/s)	Δ(I ΔV) (K km/s)
C	<sup>13</sup> CO	1 – 0	110.201	541.15	6.82	41.32	0.55
C	CH <sub>3</sub> CN	6 <sub>k</sub> – 5 <sub>k</sub>	110.383	21.96	6.8	2.69	0.55
C	CN	1 <sub>3/2</sub> – 0 <sub>1/2</sub>	113.191	196.54	23.58	33.0	2.11
C	CN	1 <sub>1/2</sub> – 0 <sub>1/2</sub>	113.491	441.29	23.45	62.01	2.1
C	H <sub>2</sub> CO	3 <sub>0,3</sub> – 2 <sub>0,2</sub>	218.222	26.6	5.74	2.39	0.52
C	H <sub>2</sub> CO	3 <sub>2,2</sub> – 2 <sub>2,1</sub>	218.476	16.17	5.72	1.67	0.52
C	C <sup>18</sup> O	2 – 1	219.56	197.0	5.67	14.75	0.52
C	<sup>13</sup> CO	2 – 1	220.399	576.38	7.98	47.41	0.72
C	CH <sub>3</sub> CCH	13 <sub>k</sub> – 12 <sub>k</sub>	222.167	23.7	7.85	2.59	0.71
C	C <sup>17</sup> O	2 – 1	224.714	21.54	6.78	1.09	0.61
C	H <sub>2</sub> CO	3 <sub>1,2</sub> – 2 <sub>1,1</sub>	225.698	39.06	6.72	1.28	0.6
C	CN	2 <sub>3/2</sub> – 1 <sub>3/2</sub>	226.36	28.52	6.68	4.11	0.6
C	CN	2 <sub>3/2</sub> – 1 <sub>1/2</sub>	226.66	98.48	6.66	14.13	0.6
C	CN	2 <sub>5/2</sub> – 1 <sub>3/2</sub>	226.875	187.62	6.65	21.08	0.59
C	CH <sub>3</sub> CCH	14 <sub>k</sub> – 13 <sub>k</sub>	239.252	22.52	7.03	0.23	0.61
C	CH <sub>3</sub> OH	5 <sub>k</sub> – 4 <sub>k</sub>	241.791	63.94	6.35	5.95	0.55
C	CS	5 – 4	244.936	56.25	7.14	5.37	0.62
C	NO	5/2 + – 3/2 –	250.483	25.51	5.83	2.1	0.5
C	NO	5/2 – – 3/2 +	250.817	18.56	6.87	0.37	0.58
C	CH <sub>3</sub> CCH	15 <sub>k</sub> – 14 <sub>k</sub>	256.337	17.95	5.71	1.29	0.48
C	CH <sub>3</sub> OH	2 <sub>1,1</sub> – 1 <sub>0,1</sub>	261.806	35.11	5.86	3.05	0.49
C	CCH	3 – 2	262.004	86.62	5.85	11.52	0.49
C	HCN	3 – 2	265.886	212.11	7.34	19.24	0.61
C	HCO <sup>+</sup>	3 – 2	267.558	439.54	7.25	44.61	0.6
C	HNC	3 – 2	271.981	60.43	6.09	4.71	0.5
C	CH <sub>3</sub> CCH	16 <sub>k</sub> – 15 <sub>k</sub>	273.42	13.82	6.05	0.76	0.49
TNE	H <sup>13</sup> CO <sup>+</sup>	1 – 0	86.754	28.32	10.67	3.21	0.98
TNE	CCH	1 <sub>3/2</sub> – 0 <sub>1/2</sub>	87.317	162.65	10.54	17.15	0.96
TNE	CCH	1 <sub>1/2</sub> – 0 <sub>1/2</sub>	87.402	87.83	10.52	9.6	0.96
TNE	HNCO	4 <sub>0,4</sub> – 3 <sub>0,3</sub>	87.926	24.61	10.39	1.06	0.94
TNE	HCN	1 – 0	88.634	459.05	10.91	37.29	0.99
TNE	HCO <sup>+</sup>	1 – 0	89.189	844.66	10.78	71.87	0.97
TNE	HNC	1 – 0	90.664	219.31	9.79	16.38	0.88
TNE	HC <sub>3</sub> N	10 – 9	90.979	25.18	9.73	1.3	0.87
TNE	CH <sub>3</sub> OH	2 <sub>k</sub> – 1 <sub>k</sub>	96.741	68.40	7.87	4.33	0.68
TNE	CS	2 – 1	97.981	150.52	7.68	12.45	0.66
TNE	H40α	—	99.023	25.57	9.81	2.77	0.84
TNE	SO	2 <sub>1</sub> – 3 <sub>2</sub>	99.3	39.38	9.76	2.49	0.83
TNE	HC <sub>3</sub> N	11 – 10	100.076	41.96	9.61	2.93	0.82
TNE	CH <sub>3</sub> CCH	6 <sub>k</sub> – 5 <sub>k</sub>	102.548	74.84	8.53	4.68	0.72
TNE	CH <sub>3</sub> OH	0 <sub>0,0</sub> – 1 <sub>1,1</sub>	108.894	26.31	7.30	2.07	0.60

*Table 13 continued*

**Table 13** (*continued*)

Position	Species	Transitions	Restfreq (GHz)	I <sub>peak</sub> (mK)	ΔI <sub>peak</sub> (mK)	I ΔV (K km/s)	Δ(I ΔV) (K km/s)
TNE	HC <sub>3</sub> N	12 – 11	109.174	16.43	7.26	0.91	0.59
TNE	SO	2 <sub>3</sub> – 1 <sub>2</sub>	109.252	17.71	7.25	0.87	0.59
TNE	C <sup>18</sup> O	1 – 0	109.782	78.58	7.19	5.69	0.58
TNE	HNCO	5 <sub>0,5</sub> – 4 <sub>0,4</sub>	109.906	23.25	7.17	1.61	0.58
TNE	<sup>13</sup> CO	1 – 0	110.201	449.06	7.13	35.71	0.58
TNE	CN	1 <sub>3/2</sub> – 0 <sub>1/2</sub>	113.191	96.05	24.71	9.16	2.21
TNE	CN	1 <sub>1/2</sub> – 0 <sub>1/2</sub>	113.491	205.02	24.59	15.34	2.2
TNE	c-C <sub>3</sub> H <sub>2</sub>	6 <sub>k</sub> – 5 <sub>k</sub>	217.822	17.86	6.86	0.78	0.63
TNE	c-C <sub>3</sub> H <sub>2</sub>	5 <sub>2,4</sub> – 4 <sub>1,3</sub>	218.16	18.62	6.84	1.71	0.62
TNE	H <sub>2</sub> CO	3 <sub>0,3</sub> – 2 <sub>0,2</sub>	218.222	18.61	6.84	1.55	0.62
TNE	C <sup>18</sup> O	2 – 1	219.56	108.09	6.77	6.92	0.62
TNE	<sup>13</sup> CO	2 – 1	220.399	550.16	9.54	42.02	0.87
TNE	CH <sub>3</sub> CCH	13 <sub>k</sub> – 12 <sub>k</sub>	222.167	42.72	9.42	2.38	0.85
TNE	H <sub>2</sub> CO	3 <sub>1,2</sub> – 2 <sub>1,1</sub>	225.698	29.55	8.1	2.4	0.73
TNE	CN	2 <sub>3/2</sub> – 1 <sub>3/2</sub>	226.36	23.01	8.07	0.21	0.72
TNE	CN	2 <sub>3/2</sub> – 1 <sub>1/2</sub>	226.66	34.19	8.05	1.24	0.72
TNE	CN	2 <sub>5/2</sub> – 1 <sub>3/2</sub>	226.875	123.5	8.04	6.89	0.72
TNE	CH <sub>3</sub> CCH	14 <sub>k</sub> – 13 <sub>k</sub>	239.252	37.16	8.68	2.3	0.76
TNE	CH <sub>3</sub> OH	5 <sub>k</sub> – 4 <sub>k</sub>	241.791	35.34	7.87	2.11	0.68
TNE	CS	5 – 4	244.936	28.97	8.91	2.05	0.77
TNE	NO	5/2 + – 3/2 –	250.483	25.95	7.34	-0.01	0.62
TNE	NO	5/2 – – 3/2 +	250.817	20.85	8.67	0.37	0.74
TNE	CH <sub>3</sub> OH	2 <sub>0,2</sub> – 1 <sub>-1,1</sub>	254.015	15.59	8.5	0.46	0.72
TNE	CH <sub>3</sub> CCH	15 <sub>k</sub> – 14 <sub>k</sub>	256.337	33.82	7.27	2.3	0.61
TNE	H <sup>13</sup> CO <sup>+</sup>	3 – 2	260.255	21.65	7.26	1.03	0.61
TNE	CH <sub>3</sub> OH	2 <sub>1,1</sub> – 1 <sub>0,1</sub>	261.806	20.93	7.55	1.34	0.63
TNE	CCH	3 – 2	262.004	68.71	7.54	6.15	0.63
TNE	HCN	3 – 2	265.886	90.5	9.52	5.88	0.79
TNE	HCO <sup>+</sup>	3 – 2	267.558	360.03	9.43	23.59	0.78
TNE	HNC	3 – 2	271.981	44.21	7.99	3.07	0.65
TNE	CH <sub>3</sub> CCH	16 <sub>k</sub> – 15 <sub>k</sub>	273.42	14.3	7.96	0.97	0.65
TSE	CCH	1 <sub>3/2</sub> – 0 <sub>1/2</sub>	87.317	95.59	10.42	10.02	0.95
TSE	CCH	1 <sub>1/2</sub> – 0 <sub>1/2</sub>	87.402	44.34	10.4	6.83	0.95
TSE	HCN	1 – 0	88.634	330.75	10.78	36.63	0.98
TSE	HCO <sup>+</sup>	1 – 0	89.189	560.87	10.65	70.52	0.96
TSE	HNC	1 – 0	90.664	123.88	9.67	13.8	0.87
TSE	N <sub>2</sub> H <sup>+</sup>	1 – 0	93.176	65.16	24.52	4.32	2.16
TSE	CH <sub>3</sub> OH	2 <sub>k</sub> – 1 <sub>k</sub>	96.741	82.94	7.76	7.93	0.67
TSE	CS	2 – 1	97.981	143.78	7.57	15.96	0.65
TSE	SO	2 <sub>1</sub> – 3 <sub>2</sub>	99.3	44.24	9.61	3.24	0.82
TSE	CH <sub>3</sub> CCH	6 <sub>k</sub> – 5 <sub>k</sub>	102.548	27.33	8.4	0.45	0.71

*Table 13 continued*



**Table 13** (*continued*)

Position	Species	Transitions	Restfreq (GHz)	I <sub>peak</sub> (mK)	ΔI <sub>peak</sub> (mK)	I ΔV (K km/s)	Δ(I ΔV) (K km/s)
TSE	C <sup>18</sup> O	1 – 0	109.782	45.97	7.06	5.73	0.57
TSE	<sup>13</sup> CO	1 – 0	110.201	292.94	7.01	31.98	0.57
TSE	CH <sub>3</sub> CN	6 <sub>k</sub> – 5 <sub>k</sub>	110.383	22.06	6.98	2.05	0.57
TSE	CN	1 <sub>3/2</sub> – 0 <sub>1/2</sub>	113.191	71.36	24.25	10.04	2.17
TSE	CN	1 <sub>1/2</sub> – 0 <sub>1/2</sub>	113.491	136.68	24.12	14.94	2.16
TSE	H <sub>2</sub> CO	3 <sub>0,3</sub> – 2 <sub>0,2</sub>	218.222	12.03	6.37	0.96	0.58
TSE	C <sup>18</sup> O	2 – 1	219.56	30.01	6.3	3.21	0.57
TSE	<sup>13</sup> CO	2 – 1	220.399	297.26	8.87	29.8	0.81
TSE	CH <sub>3</sub> CCH	13 <sub>k</sub> – 12 <sub>k</sub>	222.167	20.33	8.75	0.21	0.79
TSE	H <sub>2</sub> CO	3 <sub>1,2</sub> – 2 <sub>1,1</sub>	225.698	26.95	7.51	1.3	0.67
TSE	CN	2 <sub>3/2</sub> – 1 <sub>1/2</sub>	226.66	27.88	7.45	0.85	0.67
TSE	CN	2 <sub>5/2</sub> – 1 <sub>3/2</sub>	226.875	48.68	7.44	3.32	0.67
TSE	CH <sub>3</sub> OH	5 <sub>k</sub> – 4 <sub>k</sub>	241.791	35.04	7.22	4.07	0.63
TSE	CS	5 – 4	244.936	30.26	8.15	0.68	0.7
TSE	CH <sub>3</sub> OH	2 <sub>1,1</sub> – 1 <sub>0,1</sub>	261.806	29.02	6.81	2.49	0.57
TSE	CCH	3 – 2	262.004	24.84	6.8	0.23	0.57
TSE	HCN	3 – 2	265.886	69.33	8.57	6.13	0.71
TSE	HCO <sup>+</sup>	3 – 2	267.558	178.16	8.48	17.21	0.7
TSE	HNC	3 – 2	271.981	20.38	7.16	2.22	0.58
TSW	SiO	2 – 1	86.847	31.41	10.6	3.95	0.97
TSW	CCH	1 <sub>3/2</sub> – 0 <sub>1/2</sub>	87.317	148.27	10.49	17.04	0.96
TSW	CCH	1 <sub>1/2</sub> – 0 <sub>1/2</sub>	87.402	95.46	10.47	8.64	0.95
TSW	HNCO	4 <sub>0,4</sub> – 3 <sub>0,3</sub>	87.926	69.09	10.35	5.53	0.94
TSW	HCN	1 – 0	88.634	496.89	10.86	51.9	0.98
TSW	HCO <sup>+</sup>	1 – 0	89.189	688.99	10.73	84.51	0.97
TSW	HNC	1 – 0	90.664	202.15	9.74	17.53	0.87
TSW	HC <sub>3</sub> N	10 – 9	90.979	27.63	9.68	1.77	0.86
TSW	N <sub>2</sub> H <sup>+</sup>	1 – 0	93.176	83.15	24.71	6.26	2.18
TSW	C <sup>34</sup> S	1 – 0	96.413	29.57	7.88	2.09	0.68
TSW	CH <sub>3</sub> OH	2 <sub>k</sub> – 1 <sub>k</sub>	96.741	222.31	7.83	15.4	0.68
TSW	CS	2 – 1	97.981	187.28	7.64	15.6	0.66
TSW	SO	2 <sub>1</sub> – 3 <sub>2</sub>	99.3	46.56	9.7	4.29	0.83
TSW	HC <sub>3</sub> N	11 – 10	100.076	28.13	9.55	2.46	0.81
TSW	CH <sub>3</sub> CCH	6 <sub>k</sub> – 5 <sub>k</sub>	102.548	28.19	8.48	2.63	0.71
TSW	HC <sub>3</sub> N	12 – 11	109.174	23.39	7.21	1.2	0.59
TSW	C <sup>18</sup> O	1 – 0	109.782	95.16	7.13	6.26	0.58
TSW	HNCO	5 <sub>0,5</sub> – 4 <sub>0,4</sub>	109.906	54.65	7.12	2.54	0.58
TSW	<sup>13</sup> CO	1 – 0	110.201	381.66	7.08	29.99	0.57
TSW	CN	1 <sub>3/2</sub> – 0 <sub>1/2</sub>	113.191	76.31	24.52	4.41	2.2
TSW	CN	1 <sub>1/2</sub> – 0 <sub>1/2</sub>	113.491	201.53	24.4	18.96	2.18
TSW	C <sup>18</sup> O	2 – 1	219.56	48.71	6.57	2.99	0.6

*Table 13 continued*

**Table 13** (*continued*)

Position	Species	Transitions	Restfreq (GHz)	I <sub>peak</sub> (mK)	ΔI <sub>peak</sub> (mK)	I ΔV (K km/s)	Δ(I ΔV) (K km/s)
TSW	<sup>13</sup> CO	2 – 1	220.399	304.86	9.26	17.61	0.84
TSW	H <sub>2</sub> CO	3 <sub>1,2</sub> – 2 <sub>1,1</sub>	225.698	17.04	7.86	1.18	0.7
TSW	CN	2 <sub>3/2</sub> – 1 <sub>3/2</sub>	226.36	13.95	7.82	0.27	0.7
TSW	CN	2 <sub>3/2</sub> – 1 <sub>1/2</sub>	226.66	26.37	7.8	1.84	0.7
TSW	CN	2 <sub>5/2</sub> – 1 <sub>3/2</sub>	226.875	67.62	7.79	3.85	0.7
TSW	CH <sub>3</sub> OH	5 <sub>k</sub> – 4 <sub>k</sub>	241.791	50.67	7.6	2.5	0.66
TSW	CS	5 – 4	244.936	19.23	8.59	-0.21	0.74
TSW	CH <sub>3</sub> OH	2 <sub>0,2</sub> – 1 <sub>-1,1</sub>	254.015	23.75	8.17	0.57	0.69
TSW	CCH	3 – 2	262.004	19.45	7.23	0.23	0.6
TSW	HCN	3 – 2	265.886	81.2	9.12	4.14	0.75
TSW	HCO <sup>+</sup>	3 – 2	267.558	155.94	9.03	10.14	0.74
TSW	HNC	3 – 2	271.981	23.86	7.64	2.05	0.62
OS	SiO	2 – 1	86.847	29.29	10.57	3.83	0.97
OS	CCH	1 <sub>3/2</sub> – 0 <sub>1/2</sub>	87.317	52.69	10.46	9.79	0.95
OS	CCH	1 <sub>1/2</sub> – 0 <sub>1/2</sub>	87.402	39.54	10.44	4.01	0.95
OS	HCN	1 – 0	88.634	228.92	10.83	40.42	0.98
OS	HCO <sup>+</sup>	1 – 0	89.189	369.77	10.7	64.6	0.97
OS	HOC <sup>+</sup>	1 – 0	89.487	21.55	10.63	0.92	0.96
OS	HNC	1 – 0	90.664	90.76	9.71	12.34	0.87
OS	CH <sub>3</sub> OH	2 <sub>k</sub> – 1 <sub>k</sub>	96.741	57.49	7.8	8.35	0.68
OS	CS	2 – 1	97.981	83.96	7.61	10.34	0.66
OS	SO	2 <sub>1</sub> – 3 <sub>2</sub>	99.3	25.86	9.66	2.1	0.83
OS	C <sup>18</sup> O	1 – 0	109.782	34.8	7.1	3.44	0.58
OS	<sup>13</sup> CO	1 – 0	110.201	117.67	7.05	10.91	0.57
OS	CN	1 <sub>3/2</sub> – 0 <sub>1/2</sub>	113.191	68.06	24.41	13.07	2.19
OS	CN	1 <sub>1/2</sub> – 0 <sub>1/2</sub>	113.491	118.29	24.28	19.56	2.17
OS	C <sup>18</sup> O	2 – 1	219.56	17.85	6.46	0.77	0.59
OS	<sup>13</sup> CO	2 – 1	220.399	113.47	9.1	7.07	0.83
OS	CN	2 <sub>3/2</sub> – 1 <sub>1/2</sub>	226.66	27.86	7.65	2.21	0.69
OS	CN	2 <sub>5/2</sub> – 1 <sub>3/2</sub>	226.875	38.21	7.64	6.55	0.68
OS	CH <sub>3</sub> OH	5 <sub>k</sub> – 4 <sub>k</sub>	241.791	37.05	7.44	5.48	0.64
OS	CS	5 – 4	244.936	22.38	8.4	-0.13	0.72
OS	CCH	3 – 2	262.004	23.6	7.05	1.99	0.59
OS	HCN	3 – 2	265.886	54.12	8.88	7.3	0.73
OS	HCO <sup>+</sup>	3 – 2	267.558	95.61	8.8	11.99	0.72
OS	HOC <sup>+</sup>	3 – 2	268.451	19.6	8.75	1.41	0.72
SW	H <sup>13</sup> CO <sup>+</sup>	1 – 0	86.754	45.52	10.44	3.78	0.96
SW	SiO	2 – 1	86.847	54.12	10.42	4.69	0.95
SW	CCH	1 <sub>3/2</sub> – 0 <sub>1/2</sub>	87.317	314.32	10.31	38.99	0.94
SW	CCH	1 <sub>1/2</sub> – 0 <sub>1/2</sub>	87.402	158.32	10.29	17.79	0.94
SW	HNCO	4 <sub>0,4</sub> – 3 <sub>0,3</sub>	87.926	56.2	10.17	3.52	0.92

*Table 13 continued*

**Table 13** (*continued*)

Position	Species	Transitions	Restfreq (GHz)	I <sub>peak</sub> (mK)	ΔI <sub>peak</sub> (mK)	I ΔV (K km/s)	Δ(I ΔV) (K km/s)
SW	HCN	1 – 0	88.634	745.59	10.67	76.73	0.97
SW	HCO <sup>+</sup>	1 – 0	89.189	1106.6	10.54	124.11	0.95
SW	HOC <sup>+</sup>	1 – 0	89.487	47.47	10.47	5.01	0.94
SW	HNC	1 – 0	90.664	371.75	9.57	33.33	0.86
SW	HC <sub>3</sub> N	10 – 9	90.979	69.12	9.5	5.0	0.85
SW	N <sub>2</sub> H <sup>+</sup>	1 – 0	93.176	117.54	24.24	6.76	2.14
SW	C <sup>34</sup> S	1 – 0	96.413	22.23	7.72	2.55	0.67
SW	CH <sub>3</sub> OH	2 <sub>k</sub> – 1 <sub>k</sub>	96.741	226.19	7.67	16.09	0.66
SW	CS	2 – 1	97.981	362.43	7.48	31.55	0.64
SW	H40α	—	99.023	19.93	9.54	0.35	0.82
SW	SO	2 <sub>1</sub> – 3 <sub>2</sub>	99.3	96.97	9.49	7.96	0.81
SW	HC <sub>3</sub> N	11 – 10	100.076	49.29	9.34	5.13	0.8
SW	CH <sub>3</sub> CCH	6 <sub>k</sub> – 5 <sub>k</sub>	102.548	108.85	8.28	7.71	0.7
SW	CH <sub>3</sub> OH	0 <sub>0,0</sub> – 1 <sub>1,1</sub>	108.894	40.65	7.06	2.88	0.58
SW	HC <sub>3</sub> N	12 – 11	109.174	39.1	7.02	3.84	0.57
SW	C <sup>18</sup> O	1 – 0	109.782	145.68	6.95	11.28	0.56
SW	HNCO	5 <sub>0,5</sub> – 4 <sub>0,4</sub>	109.906	42.04	6.93	3.43	0.56
SW	<sup>13</sup> CO	1 – 0	110.201	942.81	6.89	71.38	0.56
SW	CN	1 <sub>3/2</sub> – 0 <sub>1/2</sub>	113.191	179.74	23.84	24.35	2.13
SW	CN	1 <sub>1/2</sub> – 0 <sub>1/2</sub>	113.491	374.89	23.71	42.88	2.12
SW	c-C <sub>3</sub> H <sub>2</sub>	3 <sub>3,0</sub> – 2 <sub>2,1</sub>	216.279	22.71	6.08	1.14	0.56
SW	H <sub>2</sub> CO	3 <sub>0,3</sub> – 2 <sub>0,2</sub>	218.222	26.21	5.98	2.93	0.55
SW	H <sub>2</sub> CO	3 <sub>2,2</sub> – 2 <sub>2,1</sub>	218.476	21.41	5.96	1.46	0.54
SW	C <sup>18</sup> O	2 – 1	219.56	168.14	5.91	11.45	0.54
SW	<sup>13</sup> CO	2 – 1	220.399	1009.89	8.32	75.17	0.76
SW	CH <sub>3</sub> CCH	13 <sub>k</sub> – 12 <sub>k</sub>	222.167	39.65	8.19	2.86	0.74
SW	C <sup>17</sup> O	2 – 1	224.714	37.07	7.08	3.26	0.64
SW	H <sub>2</sub> CO	3 <sub>1,2</sub> – 2 <sub>1,1</sub>	225.698	54.69	7.02	4.33	0.63
SW	CN	2 <sub>3/2</sub> – 1 <sub>3/2</sub>	226.36	21.52	6.98	3.04	0.63
SW	CN	2 <sub>3/2</sub> – 1 <sub>1/2</sub>	226.66	85.01	6.96	6.79	0.62
SW	CN	2 <sub>5/2</sub> – 1 <sub>3/2</sub>	226.875	157.89	6.95	15.05	0.62
SW	CH <sub>3</sub> CCH	14 <sub>k</sub> – 13 <sub>k</sub>	239.252	36.7	7.38	2.91	0.64
SW	CH <sub>3</sub> OH	5 <sub>k</sub> – 4 <sub>k</sub>	241.791	79.12	6.68	7.88	0.58
SW	CS	5 – 4	244.936	70.96	7.52	2.75	0.65
SW	NO	5/2 + – 3/2 –	250.483	17.52	6.15	1.75	0.52
SW	NO	5/2 – – 3/2 +	250.817	16.94	7.26	0.89	0.62
SW	CH <sub>3</sub> CCH	15 <sub>k</sub> – 14 <sub>k</sub>	256.337	24.03	6.04	1.14	0.51
SW	CH <sub>3</sub> OH	2 <sub>1,1</sub> – 1 <sub>0,1</sub>	261.806	38.48	6.22	2.64	0.52
SW	CCH	3 – 2	262.004	96.45	6.21	12.31	0.52
SW	HCN	3 – 2	265.886	163.25	7.8	12.26	0.64
SW	HCO <sup>+</sup>	3 – 2	267.558	403.21	7.71	35.26	0.64
SW	HNC	3 – 2	271.981	71.28	6.49	4.75	0.53
SW	CH <sub>3</sub> CCH	16 <sub>k</sub> – 15 <sub>k</sub>	273.42	21.45	6.45	2.79	0.53